THERMO-MECHANICAL
DESIGN AND RELIABILITY OF HIGH-PERFORMANCE
ULTRA-THIN VAPOR CHAMBERS

A DISSERTATION

SUBMITTED TO THE DEPARTMENT OF MECHANICAL ENGINEERING

AND THE COMMITTEE ON GRADUATE STUDIES

OF STANFORD UNIVERSITY

IN PARTIAL FULFILLMENT OF THE REQUIREMENTS

FOR THE DEGREE OF

DOCTOR OF PHILOSOPHY

Farid Soroush

May 2022

© 2022 by Farid Soroush. All Rights Reserved.
Re-distributed by Stanford University under license with the author.

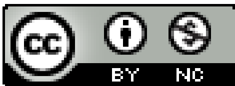

This work is licensed under a Creative Commons Attribution-Noncommercial 3.0 United States License.
http://creativecommons.org/licenses/by-nc/3.0/us/

This dissertation is online at: https://purl.stanford.edu/nw909qz5894

I certify that I have read this dissertation and that, in my opinion, it is fully adequate in scope and quality as a dissertation for the degree of Doctor of Philosophy.

Kenneth Goodson, Primary Adviser

I certify that I have read this dissertation and that, in my opinion, it is fully adequate in scope and quality as a dissertation for the degree of Doctor of Philosophy.

Roger Howe

I certify that I have read this dissertation and that, in my opinion, it is fully adequate in scope and quality as a dissertation for the degree of Doctor of Philosophy.

Thomas Kenny

Approved for the Stanford University Committee on Graduate Studies.

Stacey F. Bent, Vice Provost for Graduate Education

This signature page was generated electronically upon submission of this dissertation in electronic format. An original signed hard copy of the signature page is on file in University Archives.

Abstract

Silicon-based vapor chambers are an appealing choice for electronics cooling application due to their low thermal resistance and ease of system-level integration. However, challenges in high heat flux applications necessitates development of high-performance evaporator wicks for these two-phase cooling solutions. Here, we design, fabricate, and characterize a novel hybrid microporous evaporator wick capable of removing >150 W from 5×5 mm^2 hotspot (>600 Wcm^{-2} heat flux with thermal resistance of 0.02 $^oCcm^2W^{-1}$). We use copper wire meshes (CWMs) to provide liquid feeding and copper inverse opal (CIOs) for boiling.

Surface oxidation of the copper is a critical degradation mechanism that must be addressed to preserve the integrity and hydrophilicity of the wick. We systematically investigate the contact angle change of micro porous copper. To avoid hydrophobicity, we propose to pre-oxidize the copper evaporator wick to form a hydrophilic cupric oxide CuO. Furthermore, we develop a recipe for creation of a reliable superhydrophilic layer for micro porous wick application. We investigate effect of various maintenance protocols to ensure superhydrophilicity of the wick for long term functionality.

Thermo-fluidic performance of ultra-thin vapor chambers has been studied extensively in the past two decades, however; the thermo-mechanical design and reliability of these devices has not received much attention. The mechanical design and reliability of the vapor chamber is crucial for avoiding the device breakdown or leakage due to the high internal pressure. We develop a parametric model for thermo-mechanical design and structural analysis of an ultra-thin (1 mm thickness) miniature (15×15 mm^2 area) silicon vapor chamber. We study the effects of various design parameters such as cavity area, cavity thickness, and fillet radius. We introduce the circular cavity design for the vapor chamber application. To increase the mechanical reliability, we propose the implementation and study the design parameters of various mechanical support structures such as ribs, crossbars, and micro-post arrays. The critical point of the mechanical design is the evaporator-condenser bonding area. Gold-tin and gold-silicon eutectic bonding are

proposed as the bonding materials and methods. The samples and the tensile test setup are designed, fabricated, and tested specifically for the vapor chamber application. Findings of this study are largely beneficial in development of silicon-based heat spreaders, high-performance thermal rectifiers, next-generation heat routing technologies and heterogeneous two-phase cooling devices.

Acknowledgments

The past few years at Stanford have been a great experience for me to learn a lot about science, engineering, academia, and people. I got the chance to work on many different things, most importantly, myself. I want to use this chance to acknowledge some of the help and support that I received.

I want to thank the people of the United States for giving me this opportunity to study in their country and live with them. I do not think there is a particular place or opportunity that can make you reach what you want, however; this country (the bay area in particular) is truly a land of opportunities.

Stanford gave me the chance to interact with so many people from various backgrounds and I had the chance of learning every single day. I want to thank Stanford University and the School of Engineering specifically, for assisting me in my graduate studies. I would like to thank all members of the Stanford Nanofabrication Facilities (SNF) and Stanford Nano Shared Facilities (SNSF) for helping me with different aspects of my research.

I want to thank the Prof. Goodson regarding his help and guidance during my PhD program. Prof. Goodson's patience, emotional intelligence, maturity in dealing with people and social skills will always be a role model for me. I also want to thank Prof. Roger Howe and Prof. Thomas Kenny for their kind help in preparation of my greenlight meeting, defense meeting, and this dissertation.

I want to thank my friends and lab mates Dr. Tanya Liu, Alisha Piazza, Hansen Qiao, Dr. Ki Wook Jung, Qianying Wu, and Dr. Chi Zhang for helping me with the fabrications, experiments, writings and research projects. I also want to thank my other friends and the current or former members of the Stanford Nanoheat group, including Chris Perez, Jillian Anderson, Dr. Heundong Kwon, Prof. Tiwei Wei, Dr. Joseph Katz, and Joseph Schaadt for their support.

I want to thank my parents for the support they provided me. I think my childhood helped me significantly to develop perseverance, concentration, discipline, willpower, and problem-solving skills.

I want to thank my brother, Dr. Fariborz Soroush, for being an inspiration for me to do my graduate studies abroad and being a great help with his advice during my PhD program.

To Xixuan, who has been extremely patient with everything during this time and always supported me. Made me smile every time and was close by whenever I needed.

I also want to thank the government agencies and the companies that made these projects possible. The financial support for this research was provided by the National Science Foundation (NSF) Engineering Research Center for Power Optimization of Electro-Thermal Systems (POETS), Robert Bosch GmbH, Google LLC, Analog Devices Inc, and Department of Energy (DOE) Advanced Research Projects Agency-Energy (ARPA-E). Part of this work was performed at Stanford Nanofabrication Facilities (SNF) and Stanford Nano Shared Facilities (SNSF), supported by the National Science Foundation under award ECCS-2026822.

Table of Contents

Abstract iv

Acknowledgments vi

List of Tables x

List of Figures xi

Chapter 1 Introduction 1

1.1. Contact angle change of copper microporous wicks 1

1.2. High-Performance Evaporator 6

1.3. Reliable Ultra-Thin Vapor Chamber 7

1.4. Organization and scope of work 14

Chapter 2 Contact Angle Tuning of Copper Microporous Structures 15

2.1. Sample preparation 15

2.2. Contact angle tuning methods 16

2.3.1. Thermal Oxidation 16

2.3.2. Chemical Oxidation 19

2.3. Fine-tuning of the recipe 20

2.4. Long-term operation 25

Chapter 3 Fabrication and Characterization of Evaporator 29

3.1. Evaporator fabrication 29

3.1.1. Fabrication of copper wire mesh (CWM) wick 29

3.1.2. Fabrication of copper inverse opals (CIOs) on large areas 31

3.1.3. Fabrication of hybrid microporous structure 32

3.2. Evaporator characterization 38

3.2.1. Experiment Setup 38

3.2.2. Thermal tests 40

Chapter 4 Vapor Chamber Design and Reliability 43
4.1. Thermomechanical model 43
4.2. Modeling results 47
4.3. Experimental measurement of bond strength 55
Chapter 5 Conclusion and Future Work 65
5.1. Contact angle engineering 65
5.2. Hybrid Porous Wicks 65
5.3. Reliable vapor chamber 66
Bibliography 67
Appendix I: Heater/RTD fabrication and calibration 72
Appendix II: Considerations in tensile tests and modeling 75

List of Tables

Table 1 The simulation results for the maximum deformation, average deformation, and the maximum stress…

Table 2 Alkaline solution formulas from [11] are used in chemical oxidation processes to generate CuO nano/microstructures on the CIO wick.

Table 3 Various conditions, time, temperatures and contact materials for the contact angle measurements.

Table 4 Sample geometry, bonding area, and average fracture strength of the samples for Au-Sn (S1-S11) and Au-Si (T1-T11) bonding.

List of Figures

Figure 1 Wettability transition of freshly made CIOs sample from hydrophilic to hydrophobic through two different mechanisms…

Figure 2 Both random-packed microporous copper [19] and copper inverse opals [20] can provide higher permeability…

Figure 3-1 SEM images of various stages of thermal oxidation of CIO structures after firing in a furnace with temperatures…

Figure 3-2 (a) Hydrophobic oxide layer on CIO structure. (b) Chemical oxidation of the sample…

Figure 4 Chemical Oxidation of CIO samples: no significant difference in the morphology of the CuO structure was observed for oxidation…

Figure 5 Chemical Oxidation of CWM samples: no significant difference in the overall morphology of the CuO structure…

Figure 6 Fine-tuning of the recipe for CIO samples: oxidation duration of 1.5 and 3 minutes with alkaline…

Figure 7 Ultra-short nano grass can be formed over the microporous copper surface by using 1.5 minutes…

Figure 8 Contact angle measurement setup: Goniometer Rame-Hart 290 and an image processing…

Figure 9 Contact angle measurement of copper inverse opal (CIO) structure in various operating and maintenance…

Figure 10 The fabrication process of Single layer wire mesh without CIOs: after fabrication of heater and RTDs…

Figure 11 Schematic of the fabrication process of the micro porous copper using sacrificial template…

Figure 12 (a) Top view of the micro porous copper structure under scanning electron microscopy…

Figure 13 Fabrication process of the hybrid microporous structure: (a) Laser cutting of the copper wire mesh…

Figure 14 High quality hybrid microporous wicks: (a) conformal coating of CIOs on wires…

Figure 15 Fabrication challenges of hybrid microporous wick: (a) Non-uniformity of CIOs thickness in each tile…

Figure 16 Refined fabrication process to remove the bulk copper bumps: (1) Deposition of 10 nm titanium and 100 nm gold…

Figure 17 Refined fabrication process to prevent pore closure in copper wire mesh (CWM): (Top) Early…

Figure 18 (a) Schematic of the flow loop: In order to have better control on the liquid level and meniscus area, preheated water…

Figure 19 Significant enhancement in thermal performance by incorporating microporous copper in the wire…

Figure 20 Schematic of the CIO+CWM structure: The variation in the thickness of the CIOs film…

Chapter 1

Introduction

In the present chapter, we cover the previous studies on contact angle tuning, evaporator wicks and mechanical reliability for the vapor chamber application. We explain challenges and opportunities in each area and introduce the solutions moving forward. Large portions of this chapter are taken from Soroush et al., “A Hybrid Microporous Copper Structure for High Performance Capillary-driven Liquid Film Boiling”, ASME 2021 International Technical Conference and Exhibition on Packaging and Integration of Electronic and Photonic Microsystems, 2021; and Soroush et al., “A Hybrid Microporous Copper Structure for High Performance Capillary-driven Liquid Film Boiling”, ASME 2021 International Technical Conference and Exhibition on Packaging and Integration of Electronic and Photonic Microsystems, 2021

1.1. Contact angle change of copper microporous wicks

Microporous copper wicks are highly appealing for capillary wicking in passive cooling applications. To ensure the reliability of the copper micro porous structure in the capillary-fed boiling application, the evaporator wick must retain a hydrophilic contact angle during device operation. If the contact angle becomes hydrophobic, the wick will no longer be able to provide the capillary rewetting capability needed to supply liquid to the heated area. While freshly fabricated copper has an inherently hydrophilic contact angle, the wettability of the surface can quickly degrade [1-11] through two primary mechanisms: surface adsorption of organic contaminants or oxidation to form cuprous oxide (Cu_2O). As shown in Figure 1, a freshly fabricated CIO structure will become hydrophobic after exposure to ambient conditions for approximately 2 days. We observed that the hydrophilicity of the structure is recoverable with an O_2 plasma treatment, which implies that surface organic contamination is responsible for the hydrophobicity. If the sample is heated in ambient or water above approximately 100 ^{o}C, however; the copper will oxidize to form Cu_2O, which is apparent in the color change of the CIO structure as shown in Figure 1. As the hydrophobicity, in this case, is attributed to the surface oxidation of the structure,

it is unaffected by plasma treatment. Therefore, surface oxidation of the copper porous structures is a critical degradation mechanism that must be addressed to ensure proper functionality of the wick, particularly if using water as the working fluid of choice in the cooling device.

In the past, various methods have been used for contact angle tuning of copper surfaces. For instance, Cho et al. [1] coated copper micro pillars with 100 nm of SiO_2 nanoparticles using electron beam Physical Vapor Deposition (PVD) to enhance surface wettability and reported a decrease in the contact angle from ~90° to ~30°. Jung et al. [2] used Atomic Layer Deposition (ALD) on porous polymer films and reported a change in the contact angle from 120° to 30° by doing ALD cycles up to 100 times.

ALD and PVD methods have shown promise for the creation of a hydrophilic contact angle, however; due to the low cost and ease of implementation, thermal and chemical oxidation methods are desirable choices for contact angle tuning of copper. Chemical oxidation reactions of copper may vary significantly based on the solution type, composition, and temperature, however; the thermal oxidation reactions can be generalized as shown in Equation (1).

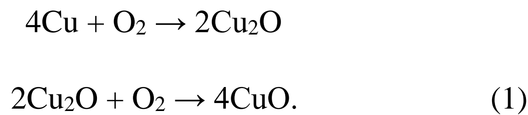

$$4Cu + O_2 \rightarrow 2Cu_2O$$
$$2Cu_2O + O_2 \rightarrow 4CuO. \quad (1)$$

At the early stages of thermal oxidation, a layer of cuprous oxide (Cu_2O) will grow. When the thickness of the Cu_2O layer surpasses 300 nm and the temperature reaches over 260 °C, the formation of the CuO layer starts. After thermal oxide growth of up to 1 μm thickness, the reaction slows down significantly due to the surface passivation with the CuO layer [6].

Oxidation methods have been studied extensively for bulk copper surfaces in the past. For example, Chang et al. [4] created CuO nanowire films from a bulk copper substrate by thermal oxidation at ~300 °C. Although the film was superhydrophilic initially, it became increasingly hydrophobic with annealing in air at 100 °C. XPS spectra before and after annealing still showed the dominant structure is CuO. The authors hypothesize that the top CuO layer surface may be partially deoxidized into Cu_2O and reported that superhydrophilicity can be recovered with annealing at 350 °C. Zhou et al.

[5] fabricated CuO structures with chemical oxidation using NaOH and $(NH_4)_2S_2O_8$ solutions on bulk copper. Then, they salinized the surface with n-hexane solution to create a superhydrophobic surface. CuO structures that were used as the condenser of a vapor chamber were peeled off after experiments. Nam et al. [6] studied the effect of 3 oxidation formulas and oxidation durations varying from 1 minute to 8 hours for bulk copper surfaces. They reported an increase in the length of the nano needles and the creation of nano flowers by increasing the oxidation duration. A reduction in the static contact angle from ~80° to ~40° was reported after heating for more than 200 minutes. Huang et al. [7] formed superhydrophilic CuO nanowires on copper after submerging in 30% wt H_2O_2 aqueous solution. Superhydrophilic CuO nanowire films showed a contact angle increase to 80° with time (unheated in the room environment). They hypothesize that the phenomenon is due to the coexistence of CuO and Cu_2O. Long et al. [8] observed the wettability transition of CuO grown over bulk copper samples after storing in different environments. They formed superhydrophilic copper surfaces from laser ablation and stored different samples in environments of CO_2, O_2, vacuum, organic, and air. They reported the most increase in the contact angle in the organic environment with the highest carbon to copper ratio, close to air. While pristine samples had a contact angle of less than 20°, samples stored in the air or the organic environment for more than 8 days showed a contact angle of over 110°. Hydrophobicity was attributed to the absorption of organics and similar to Chang et al. [4], the hydrophilic contact angle could recover after annealing at ~250 ^{o}C. Dubey et al. [9] used a combination of NaOH and $K_2S_2O_8$ to create a heterogeneous copper oxide over bulk copper surfaces with two level features and reported time evolving nanostructures started with a grass regime (up to 3 minutes of oxidation) followed by a flower regime (between 3 to 15 minutes of oxidation). Round nano grass and nano flowers were observed for NaOH-$K_2S_2O_8$, solution and $K_2S_2O_8$ solution, respectively. They reported a reduction in the contact angle and moving to flower regime from grass regime with increasing the oxidation duration.

The mentioned studies [1-9] have investigated the formation of the hydrophilic oxide (CuO) over bulk copper, while for evaporator wick application, the method used to decrease the contact angle should also have minimal impact on the permeability of the micro porous structure (CWMs or CIOs). Pham et al. [10] proposed an electrochemical

oxidation process for contact angle tuning of copper inverse opals (CIOs) with a pore diameter of 0.6 μm. They reported a stable contact angle after repeated dip and dry processes in water up to 10 trials. On the other hand, they reported a hydrophobic contact angle after heating up to over 90 ^{o}C. They conducted XPS microscopy for the electrochemically oxidized samples. XPS spectra showed a large CuO peak in the fresh samples. After heating, the contact angle increased and the sample surface became more metallic, which implies partial deoxidation of CuO may be responsible for the hydrophobicity.

Oxidation seems to be a promising approach for contact angle tuning of copper and has been studied extensively for bulk surfaces [1-9]; however, pore closure in micro porous copper structures has remained a major challenge that needs to be addressed. Additionally, the surface should retain its hydrophilic contact angle for device operating conditions such as boiling for hours in a saturated environment.

In this study (see Chapter 2), to avoid the formation of hydrophobic Cu_2O, we proposed to pre-oxidize the copper micro porous structures to form the hydrophilic cupric oxide (CuO). As Cu_2O is frequently an intermediary oxidation state between the formation of CuO from pure Cu [11], pre-oxidizing the surface to drive the reaction all the way to form CuO should result in a stable oxidation state. Here, we investigate the effect of forming a CuO layer on the surface of the porous copper samples through two different pathways: thermal and chemical oxidations. Thermal oxidation significantly changed the morphology of the micro porous copper. The oxide layer created based on this method had low mechanical stability, and the contact angle was unstable. Moving forward, two chemical oxidation formulas with various oxidation durations have been implemented to form a stable hydrophilic CuO layer on the copper surface at low temperatures (70 and 90 ^{o}C) [11] without a significant change in the morphology. The CuO layer increases hydrophilicity through the chemical bonding between the hydrogen atoms in H_2O and oxygen atoms in CuO. Additionally, the CuO nano needles increase the surface roughness which helps with the surface wettability [6]. The recipe has been optimized to have minimal impact on the porosity of the structure and prevention of the neck closure (neck diameter of ~1 μm, nano needle length of <100 nm).

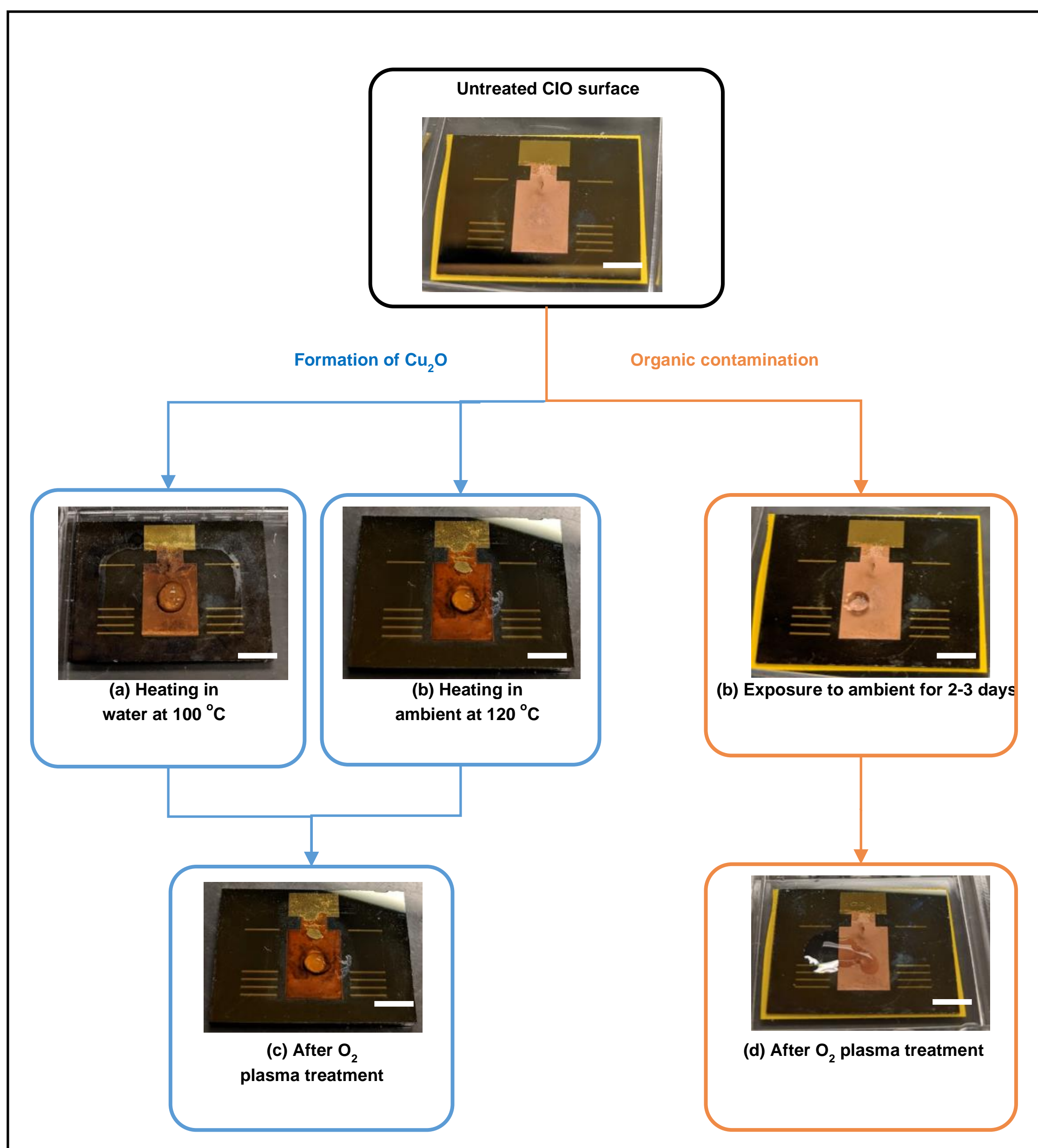

Figure 1. Wettability transition of freshly made CIOs sample from hydrophilic to hydrophobic through two different mechanisms: oxidation to form Cu_2O, and organic contamination. The hydrophilicity of the structure is recoverable with an O_2 plasma treatment if the hydrophobicity results from organic contamination. (a) Color change indicates the formation of Cu_2O, the structure becomes hydrophobic, (b) Organic contamination leads to hydrophobicity (c) Structure remains hydrophobic due to Cu_2O (d) Recovery of hydrophilicity. Scale bars are equivalent to 5 mm. Image is courtesy of Tanya Liu.

1.2. High-Performance Evaporator

Copper inverse opals with homogeneous pore sizes are highly appealing due to the ease of modeling and the potential of fabrication in hierarchal order. Chi et al. [19-20] micro fabricated and conducted systematic boiling experiments using orderly-packed Copper Inverse Opals (CIOs) that were subsequently utilized to develop an elegant model to predict both the critical heat flux (CHF) and critical wicking lengths. Recently, Wu et al. [21] demonstrated the feasibility of fabricating graded CIOs (g-CIOs) and conducted systematic modeling for design optimization of a two-layer g-CIOs [21]. The results indicated better thermal performance compared to the orderly-packed CIOs, however; given the challenges associated with microfabrication of the g-CIOs, a more robust CIOs structure with comparable or better performance is needed. A previous work by Palko et al. [18] for randomly-packed CIOs, had shown promising “experimental” results for both CHF and wicking characteristic length scale. Chi et al. [22] conducted systematic design and optimization of the randomly-packed CIOs that indicates superior performance compared to both orderly-packed [19-20] and g-CIOs [21], see Figure 2. Additional to the advantage in permeability, randomly packed CIOs are appealing from the fabrication perspective. Imperfections such as micro scale voids and cracks can be observed in the morphology of the randomly packed CIOs. This is due to the variation in the diameter of the polystyrene spheres and using ethanol as the solution (fast evaporation of the solution results in a short time for self-assembly and randomness in the structure). However, the structure of the ordered packed CIOs does not include the mentioned imperfections and polystyrene spheres in these structures are densely packed. The high packaging density of the spheres and the high order of the structure result in the vulnerability of the bonding area (between the sacrificial film and the gold seed layer) to any form of vibration. Proper handling of the orderly packed CIO samples is extremely challenging during the fabrication process due to vibrations and consequently detachment of the sacrificial film from the gold seed layer. Fabrication of the randomly packed CIOs does not face detachment challenges and is more robust.

Therefore, the present work (see Chapter 3) will utilize the randomly-packed CIOs to develop the high heat flux boiling tiles in combination with copper wire mesh as the liquid delivery microstructure. The copper wire mesh microstructure was utilized in the

past as a wicking structure where its large permeability makes it suitable to provide liquid delivery pathways to randomly-packed CIOs, see Figure 2.

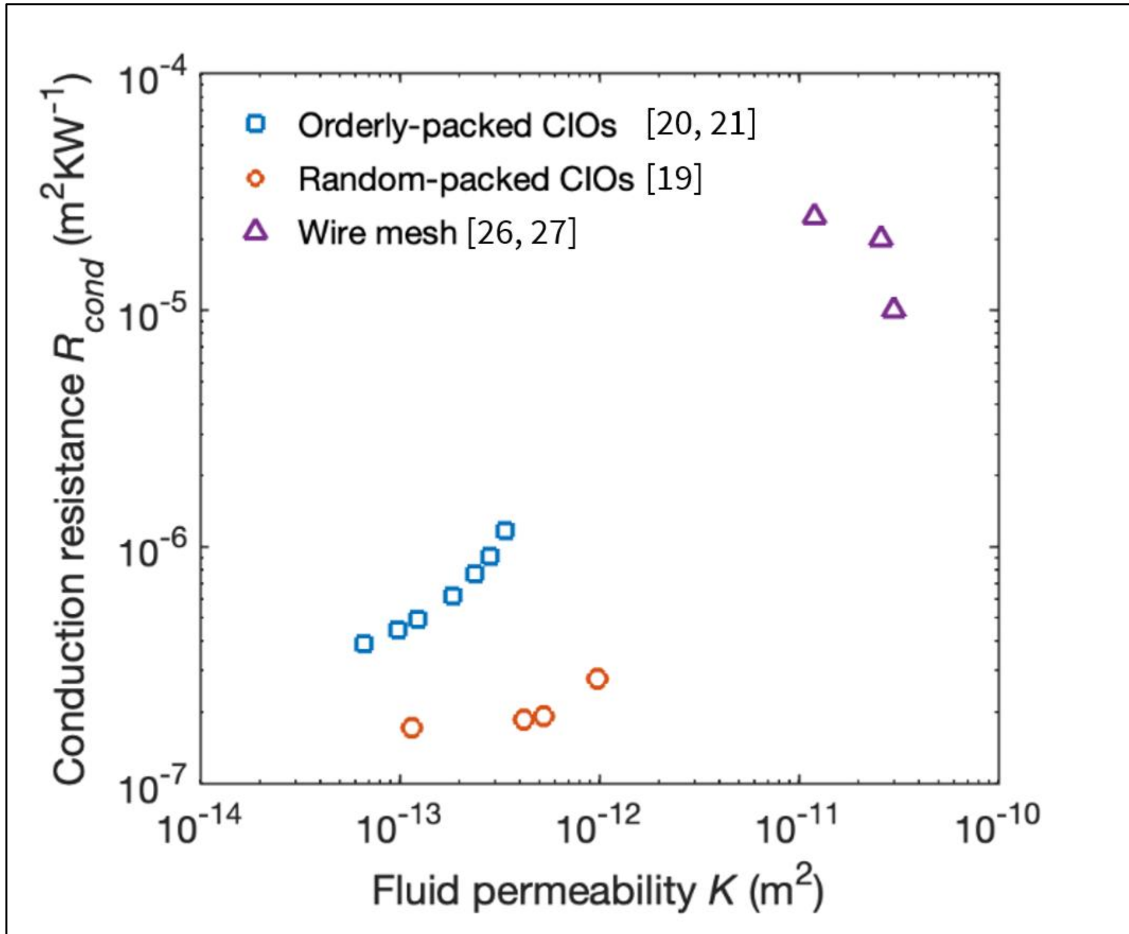

Figure 2. Both random-packed microporous copper [19] and copper inverse opals [20] can provide higher permeability, lower conduction thermal resistance, and thinner evaporator structure (appealing for the fabrication process of ultra-thin vapor chambers) compared with sintered copper [23-25] and copper wire meshes [26, 27]. Random-packed microporous copper can achieve a higher fluid permeability via template sintering compared to ordered inverse opals due to further enlargement of necks. Random-packed [22] CIOs could potentially offer comparable or better performance in comparison with “graded” CIOs [21].

1.3. Reliable Ultra-Thin Vapor Chamber

Ultra-thin silicon vapor chambers are among the most promising technologies for heat spreading in electro-thermal systems with compact packaging and high-power density

[28]. Researchers have previously studied the thermo-fluidic performance of these devices very well [29, 30]. However, challenges associated with the mechanical design and structural reliability of silicon ultra-thin vapor chambers have not received much attention. Operating temperature at 150 ^{o}C in a saturated environment with water as the working fluid will result in a vapor saturation pressure of up to ~0.5 MPa inside the of the device that might cause the breakdown of the cavity or leakage in the bonding section. The mechanical design and the integrity of the UTVC is therefore crucial for the long-term operation in this application. In the present study, we show that tolerating the high vapor pressure is challenging with the bare cavity design. To address this, implementation of the mechanical support structure can be promising, however; the employment of these structures for the vapor chamber application has not been studied well in the past. The variety of the mechanical supports (e.g. ribs, crossbars, and micro-posts array) along with the different design parameters such as dimensions, density of the support structures, and their positioning are among the factors that make this implementation very challenging. Therefore, a careful, parametric design approach is needed to increase the mechanical reliability of the device. The mechanical properties of silicon and strength of the bonding area between the evaporator and the condenser are other important points that should be considered in the mechanical design process and calculations of the safety factor.

Regarding the thermo-mechanical analysis, some scatter and preliminary models for ultra-thin vapor chambers have been developed in the past. For instance, Cai et al. [31] developed a thermo-mechanical model for a triple-stack silicon vapor chamber (38×38×3 mm3) with 8 supporting posts (2×2 mm2 area). To model the operating condition at high vapor saturation pressure, the study simulates the uniform internal pressure of 1 MPa in the cavity area. This pressure is equivalent to the saturation pressure of water at 180 ^{o}C. The paper does not provide any analysis for the bare cavity design and conducts the mechanical analysis assuming to have the 8 supporting posts. Position of the support structures plays an important role in the mechanical reliability. For instance, in the mentioned study [31], the maximum reported stress in the initial design was 462 MPa, however; the authors were able to reduce the maximum stress by ~50% by repositioning of the supporting posts. In the optimized design, the maximum stress was reported to be located on the mid-section of the cavity and the eight posts. This section is therefore the

critical point of the mechanical design for the modeled triple-stack vapor chamber and shows the importance of the mechanical strength in the evaporator-condenser boding section in the double-stack configuration (see section 4.1, Figure 21). In another study, Cai et al. [32] modeled a uniform 13×8 micro-pillar array (2 mm pillar diameter) in a 50×70×1 mm^3 silicon vapor chamber. Same as [31], the operating condition was simulated by considering a uniform pressure boundary condition. The single case of 1 MPa uniform compressive pressure was considered to simulate the operating condition with water at 125 ^{o}C. The maximum compressive stress was calculated to be much lower than the compressive strength of silicon (56 MPa vs. ~3500 MPa [34]). Therefore, the study [31] also concludes that the compressive stresses are not the main challenge in the mechanical design of the vapor chamber. In another experimental study conducted by Wei et al. [33], 4 supporting posts with the diameter of 3 mm were fabricated for a 40×40×1.25 mm^3 silicon vapor chamber. However, the study did not provide any modeling or analysis for the mechanical support structures. Lastly, although the mentioned studies [31-33] have attempted to circumvent the mechanical challenges by introducing the mechanical support posts, they did not consider the implementation of the other mechanical support structures (e.g. ribs or crossbars, etc.) or conduct a parametric study. The studies [31-33] also did not consider the bare cavity design and conducted their analysis assuming to have the support structures.

Reference values for the mechanical properties of silicon play an important role in the mechanical safety factor calculations. The mechanical strength of silicon micro-structures has been studied extensively in the past few decades. Here, we review the studies regarding compressive strength, fracture strength, Young's modules, and Poisson's ratio. We choose the conservative values (i.e. considering worst case scenario) for the mechanical safety factor calculations in the present study.

Regarding the compressive strength of silicon, Moser et al. [34] reported values ranging from 3500 to 8800 MPa for the silicon micro-posts with the aspect ratio (length/diameter) of 2.4 to 3.9. Therefore, as a conservative assumption in our study, we assume the compressive strength of silicon to be 3500 MPa.

In contrast with the compressive strength, there is a significant variation in the measured values for the fracture strength of silicon in the literature. This is due to the fact that the fracture strength of silicon varies significantly depending on the fabrication process of the wafer, surface finish, doping, and crystal orientation. Additionally, the size of the structure plays an important role in the fracture strength (e.g. varying from 10 MPa in mili-scale to 11 GPa in nano-scale) [35]. Chong et al. [36] characterized the fracture strength of silicon dice and reported that the fracture strength for the dummy wafers was higher than the prime wafers (525 MPa vs. 425 MPa and 540 MPa vs. 490 MPa for 0.155 mm and 0.3 mm die thickness, respectively). This is because of the fact that the additional fabrication process for prime wafers introduce residual stress to the wafer and reduce the mechanical strength. Moreover, the effect of the back grinding pattern was studied and the fracture strength of 300-700 MPa was reported depending on the pattern orientation. Wu et al. [37] reported that silicon wafers with (100) orientation showed ~50% higher fracture strength (3.0 vs. 2.1 GPa) compared with wafers with (111) orientation. McLaughlin et al. [38] reported fracture stress of 2.0-3.5 GPa for silicon wafers with different crystal orientations. Various surface finish methods were reported to have a significant effect on fracture stress, varying from 3.7 GPa to 8.8 GPa. For the vapor chamber application, the microfabrication process can include silicon etching, evaporation, back grinding, surface finishing, etc. Therefore, as a conservative assumption in this study, the fracture strength of silicon is assumed to be 300 MPa.

The measured values for the modulus of elasticity E can vary up to ~70% (130 GPa [39] vs. 187.5 GPa [44]). This will lead to significant variations in the calculations of the maximum deformation δ_{max}. However, here we focus on the calculation of the maximum stress σ_{max}. The effect of the Young's Modulus E and the Poisson's ratio ν on the maximum stress σ_{max} is negligible (table 1). In the present study, we assume an isotropic silicon structure and use the average values for E and ν for simplicity.

The critical point of the vapor chamber design is the bonding area between the evaporator and the condenser. The bonding strength of this section, therefore, determines the mechanical safety factor of the entire design. The strength of the bonding area is highly dependent on the bonding material and the bonding method. Gold-tin and gold-silicon

eutectic bonding are appealing choices for the ultra-thin vapor chamber application due to their low thickness (~ 1 μm), high thermal conductivity, and compatibility with micro-fabricated devices (e.g. capability of deposition over thin micro-channels or on top of the micro-pillar structures). For the ultra-thin vapor chamber application, the vapor pressure inside of the chamber will cause a tensile stress in the bonding area. Some studies in the past have investigated the fracture strength of gold-tin and gold-silicon eutectic bonding. Regarding Au-Sn eutectic bond, Turner et al. [45] measured the fracture strength of AuSn-PZT5h (for piezoelectric application) at the bonding temperature of 300 ^{o}C (80:20 Au-Sn ratio) to be 1-9 MPa. On the other hand, a recent study by Soroush et al. [46] measured the fracture strength of gold-tin bonding (80:20 Au-Sn ratio) at the temperature of 350 ^{o}C to be 3.2 MPa. We use the same Au-Sn ratio as [45, 46], however; we target the bonding temperature of 420 ^{o}C for the better diffusion of Au and Sn layers to improve the bonding strength. Regarding Au-Si eutectic bond, Wang et al [47] reported the bonding strength of ~9 MPa for Au-Si at bonding temperatures below 300 ^{o}C. The bonding temperature increase in the Au-Si eutectic bonding helps with the better diffusion of the bonding materials and strengthening the bond. For instance, Rabold et al. [48] conducted the bonding at the temperature of 400 ^{o}C (100 ^{o}C higher than [47]) and reported the fracture strength of 12 MPa for 100 nm Au layer. We target the bonding temperature of 420 ^{o}C in our study to achieve an even higher bonding strength. Regarding the layer composition in Au-Si bonding (i.e. the gold layer thickness), Nai et al. [49] performed the Au-Si bonding at the same temperature as [48] (400 ^{o}C) but with 1 μm Au layer (10 times higher thickness than [48]) and measured the fracture strength of 18 MPa. Tanaka et al. [50] observed an increase in the fracture strength from 6 MPa to 20 MPa by increasing the Au layer thickness from 0.6 μm to 1 μm. However, the strength remained unchanged for the thicknesses over 1 μm. We therefore use the gold layer thickness of 1 μm for Au-Si bonding in this letter.

In the present study, two bonding substrates are designed and fabricated that mirror the bonding cross section areas for silicon micro-post structures specifically designed for the vapor chamber application. A uniaxial tensile force has been directly applied to the samples and the fracture strength in the bonding interface is measured.

It is worth mentioning that room-temperature direct bonding of Si-Si is possible and can be explored in future studies for vapor chamber application. Si-Si direct bonding requires high vacuum and extensive surface treatment, however; it can provide a fracture strength higher than silicon [51]. A variant of this process has been commercialized recently for accelerometer fabrication [52].

In the present work (see Chapter 4), we develop a parametric model for the stress analysis in silicon vapor chamber application. We study the effect of the different design parameters such as cavity area, cavity thickness, and fillet radius on the mechanical reliability of the UTVC. To increase the mechanical reliability of the device, we propose various mechanical support structures and study their effect on increasing the safety factor. Gold-tin and gold-silicon bonding are proposed for the bonding section which is the critical part of the mechanical design. Substrates are fabricated for the vapor chamber application using the conventional microfabrication processes and then are bonded together. The tensile test setup is carefully designed, and the strength of the bonding area is characterized. The measured average bonding strength for the bonding recipe presented in this study is higher than the previous bonding recipes for both types of bonding.

Table 1. The simulation results for the maximum deformation δ_{max}, average deformation δ_{ave}, and the maximum stress σ_{max} for the baseline cavity design at the working temperature of 180 ºC with different values of Young’s modulus E and Poisson’s ratio v. As shown, the variation in E and v has a significant effect on the average δ_{ave} and the maximum δ_{max} deformation, however; it does not change the maximum principal stress σ_{max} in the structure (e.g. less than 0.2% change in σ_{max} by changing E and v by 50%).

Case ID	**Young’ s Modulus E (GPa)**	**Difference with case 1 in E (%)**	**Poisson’ s Ratio ν**	**Difference with case 1 in ν (%)**	**Maximum Deformation δ_{max} (μm)**	**Difference with case 1 in δ_{max} (%)**	**Average Deformation δ_{ave} (μm)**	**Difference with case 1 in δ_{ave} (%)**	**Maximum Principal Stress σ_{max} (MPa)**	**Difference with case 1 in σ_{max} (%)**
1	162	0	0.26	0	33.6	0	2.1	0	573.9	0
2	324	50	0.13	50	17.7	47.31	1.1	47.28	574.9	0.2
3	202	19.8	0.22	15.4	27.5	18.17	1.7	18.14	574.3	0.1

1.4. Organization and scope of work

Chapter 1 introduces the challenges and opportunities in electronics cooling application related to contact angle engineering, evaporator wicks and thermo-mechanical design. The proposed solution and the overall approach in each area are briefly discussed.

Chapter 2 dives deeper into the process of contact angle tuning with explaining the sample preparation steps, thermal and chemical oxidation methods, advantages and disadvantages of each method, fine-tuning of the recipes for copper microporous wick application, and developing a cleaning protocol for the device application in long-term operating condition.

Chapter 3 extensively discusses the detailed fabrication steps for the high-performance evaporator wick, silicon chip design and fabrication, thermal test rig, and thermal performance results.

Chapter 4 covers the silicon vapor chamber design and reliability, thermomechanical model, result of the simulations, sample design and fabrication process for the experimental measurements, gold-tin and gold-silicon eutectic bonding, tensile test setup, and fracture strength measurements.

Chapter 5 summarizes and concludes the findings of for the hydrophilicity study, boiling tests and reliability measurements. The pain points and future steps for each area are explained in this section. Additional research directions are proposed for future electronics cooling schemes using two-phase thermal management devices.

Chapter 2
Contact Angle Tuning of Copper Microporous Structures

In this chapter, we systematically investigate the contact angle change of untreated copper and various copper oxides under different conditions. To avoid the formation of hydrophobic Cu_2O, we pre-oxidize the copper micro porous wick to form hydrophilic cupric oxide CuO and study the effect of various thermal and chemical oxidation recipes on the hydrophilicity and morphology of the resulting structures. A chemical oxidation formula is implemented for the creation of a stable superhydrophilic surface at a low temperature (70 ^oC) for copper inverse opals (CIOs) (5 μm pore size) and copper wire meshes (CWMs) (76 μm pore opening). The recipe has been optimized to create nano CuO needles with a length of <100 nm and keep the necks (~1 μm diameter) open for better capillary wicking of the working fluid. Large portions of this chapter are taken from Soroush et al., "A Hybrid Microporous Copper Structure for High Performance Capillary-driven Liquid Film Boiling", ASME 2021 International Technical Conference and Exhibition on Packaging and Integration of Electronic and Photonic Microsystems, 2021.

2.1. Sample preparation

The fabrication process of copper inverse opal (CIO) samples started with a 500 µm thick 4-inch Silicon wafer. After spin coating a 1 μm thick photoresist (SPR3612) over the wafer, a rectangular seed layer pattern was exposed using a maskless exposure tool. Next, 10 nm of Titanium and 100 nm of Gold were deposited with an electron beam metal evaporator at a vacuum pressure of less than 10^{-7} Torr. Polystyrene spheres with an average diameter of 5 μm were fabricated based on dispersion polymerization [53] and sedimented over the seed layer, then sintered at 105 ^oC for more than 30 minutes. Afterward, up to 15 μm of copper was plated using an electroplating current of 10 mA for 30 minutes. Copper wire mesh (CWM) samples were purchased from TWP Inc. (part number 200X200C0020W48T) with pore opening and wire diameter of 76 and 50 μm, respectively.

Samples were cleaned for at least 3 minutes using consecutive Acetone, Isopropanol, and deionized water rinse before oxidation (see Chapter 3 page 31 for more details).

2.2. Contact angle tuning methods

Pristine micro porous copper surface has a hydrophilic contact angle [10], however; the contact angle of the surface changes significantly in the ambient environment. As shown in Figure 1, after 2-3 days of exposure to the ambient (no heating), a hydrophobic contact angle was observed for the copper inverse opal (CIO) samples. It was possible to recover the hydrophilicity using O_2 plasma treatment. Therefore, we hypothesize that the change in the contact angle is due to the adsorption of the organic contaminants. Additionally, we observed the formation of a hydrophobic contact angle after 30 minutes of heating in ambient at 120 ^oC and heating in water at 100 ^oC. In contrast to the previous case (exposure in the ambient for 2-3 days), the hydrophilic contact angle was not recovered after O_2 plasma treatment. A slight change in the color of the surface (from light purple to dark orange) was observed in this case. We hypothesize that the creation of the hydrophobic contact angle after heating is due to the formation of a cuprous oxide layer (Cu_2O) which inherently has a hydrophobic contact angle [11]. To prevent the formation of the cuprous oxide layer (Cu_2O), we propose to pre-oxidize the copper surface to create a cupric oxide layer (CuO) which inherently has a hydrophilic contact angle [11]. We implement thermal and chemical oxidations for the controlled oxidation process.

2.3.1. Thermal Oxidation

We investigated two different methods of oxidizing CIO structures to form a hydrophilic CuO layer. The first method is through a thermal oxidation process [4] where untreated CIO samples were placed into a furnace and fired at various temperatures and durations in ambient conditions.

As shown in Figure 3-1(a), firing at 200 ^oC did not show a distinct change in the morphology of the structures. A contact angle test after firing showed that the structure was hydrophobic, implying that a thin layer of Cu_2O most likely formed during the firing process. In Figure 3-1(b), a thin layer of oxide formation is visible over the CIOs pores after firing at 300 ^oC. The color of the structure appears black at this point, making it likely that some amount of CuO has now formed over the structure. Above 400 ^oC, the structure

becomes a dark black color and has a superhydrophilic nature. From the SEM images in Figures 3-1(c-f), CuO nanograss formation is observed everywhere throughout the structure. The CIOs structure does appear to deform, however; after firing at these elevated temperatures. Crisp edges start to become more rounded, and the structure appears to become more disordered. This may not necessarily be detrimental to thermal performance, however; as the permeability of the structure may increase through this method. The mechanical stability of the CuO layer formed through this method appears to be poor and the CuO layer is easily separated from the underlying Cu with a gentle scratch from a tweezer tip (Figures 3-1(g-h)). This may pose challenges for the long-term reliability of the structure, particularly in scenarios with vigorous boiling.

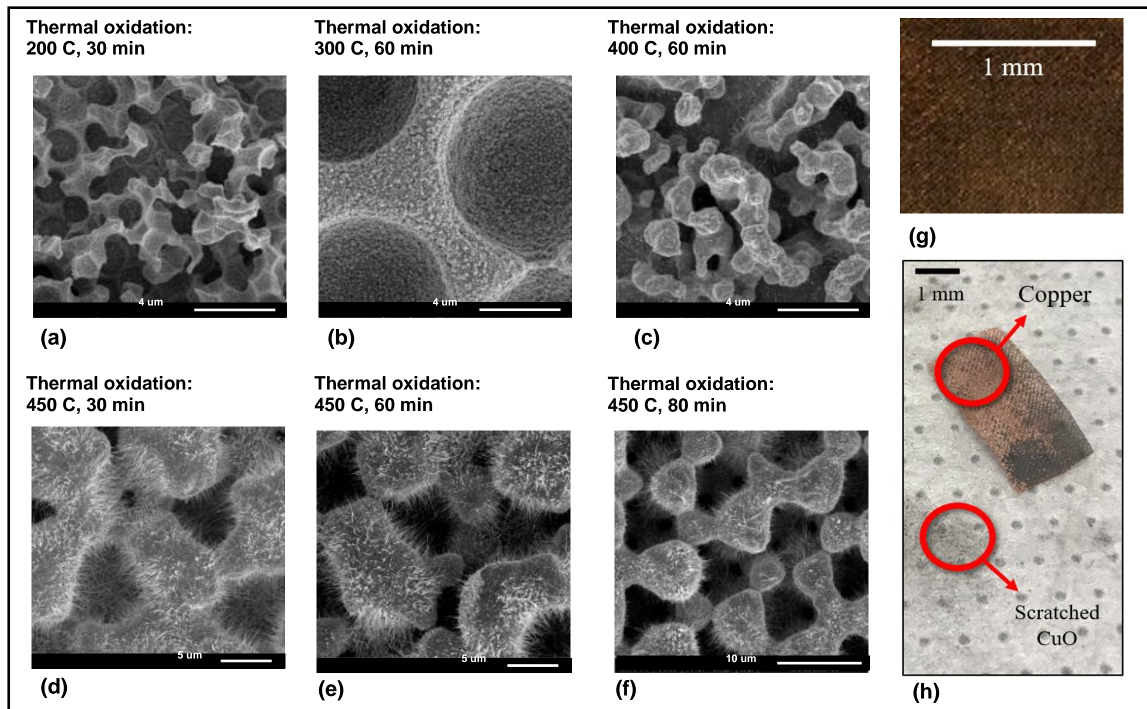

Figure 3-1: SEM images of various stages of thermal oxidation of CIO structures after firing in a furnace with temperatures ranging from 200 – 450 ^{o}C. **(a)** Firing at 200 ^{o}C appears to form a thin layer of Cu_2O and results in a hydrophobic structure. **(b)** At 300 ^{o}C, the resulting structure appears to be CuO and has a blackened appearance along with a superhydrophilic contact angle. **(c-f)** Above 400 ^{o}C, the inverse opal structure starts to deform and CuO nanograss becomes visible everywhere along the surface. The resulting structure is black in appearance and superhydrophilic. **(g)** Surface of the CWM structure after 4 hours of boiling shows instability of the thermally grown CuO coating. **(h)** Cupric oxide (CuO) layer can easily be removed from the CWM structure with a tweezer. SEMs (a-f) are courtesy of Tanya Liu.

2.3.2. Chemical Oxidation

We, therefore, explored a second method to form a hydrophilic CuO layer over the CIOs structures with a chemical oxidation approach. Two different alkaline solutions (listed in Table 2) were utilized based on the work of Nam et al. [11] to form two different types of CuO structures with distinct morphologies. As seen in Figure 3-2, alkaline solution (1) generates a distinct CuO micrograss coating over a planar copper surface. The resulting structure is superhydrophilic and maintains a stable hydrophilic contact angle for more than 48 hours of exposure in ambient conditions. The average length scale of the CuO microstructure is in the order of 1 μm, however; which is on the same order as the neck size for CIOs. As seen in Figure 3-2(b), the oxidized CIOs structure with alkaline solution (1) does not have individual neck sizes visible anymore, raising the concern that the CuO microstructures formed through this method may inhibit the fluid flow through the CIOs wick.

Table 2. Alkaline solution formulas from [11] are used in chemical oxidation processes to generate CuO nano/microstructures on the CIO wick.

Alkaline solution (1)		Alkaline solution (2)	
Component	Recipe	Component	Recipe
$NaClO_2$	3.75 g	$NaClO_2$	16 g
NaOH	5 g	NaOH	5 g
$Na_3PO_4 12H_2O$	10 g	-	
DI water	100 mL	DI water	100 mL
Temperature	90 ^oC	Temperature	70 ^oC

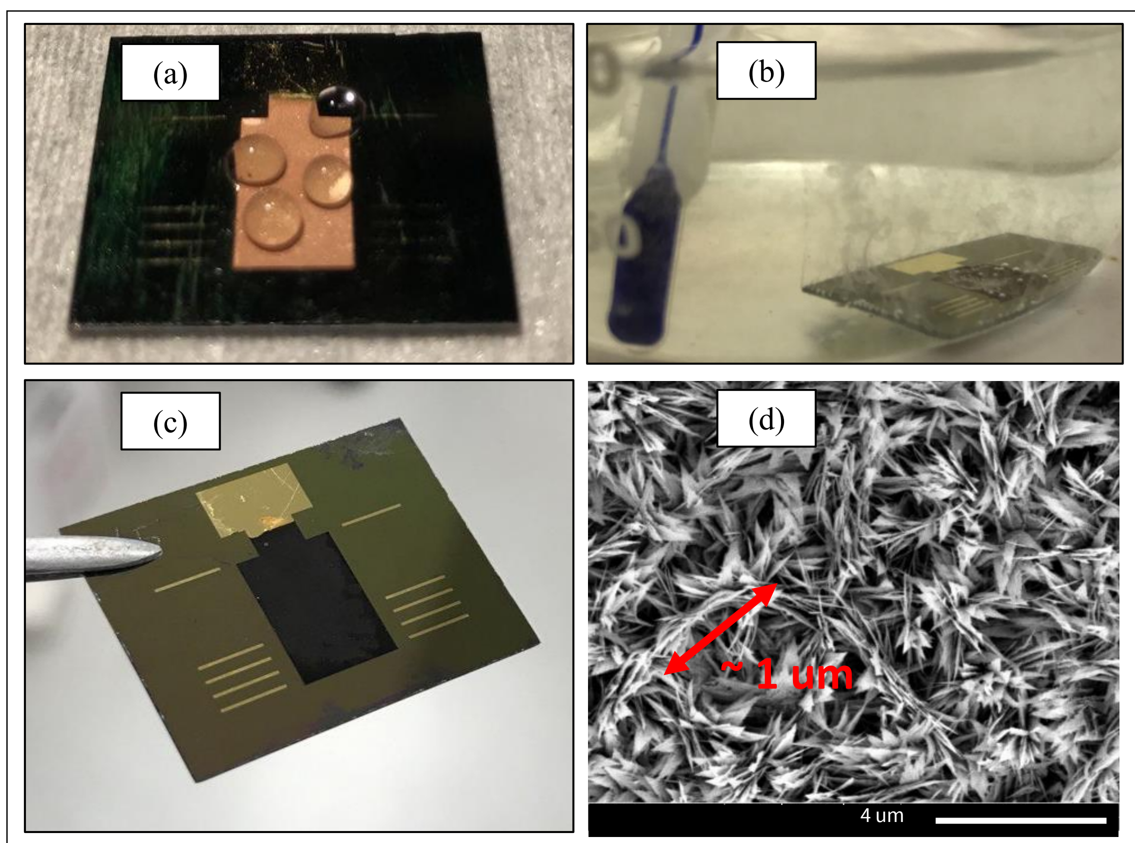

Figure 3-2: **(a)** Hydrophobic oxide layer on CIO structure. **(b)** Chemical oxidation of the sample. **(c)** CuO microstructures formed on top of a CIO surface after chemical oxidation with alkaline. solution (1). **(d)** A CIO structure after chemical oxidation with alkaline solution (1). The individual necks that link the fluid pathways between distinct pores are no longer visible and may be blocked by the CuO microstructures. SEM (d) is courtesy of Tanya Liu.

2.3. Fine-tuning of the recipe

To circumvent the pore closure issue, we investigated fine-tuning of the oxidation formulas using various oxidation durations in order to create an oxide layer with minimum impact on the permeability of the structure. As shown in Figures 4 and 5, the two chemical oxidation formulas and 4 oxidation duration (5, 10, 15, and 20 minutes) have been studied for both the CIO and CWM structures. Oxidation durations between 5 to 20 minutes did not have a significant effect on the nano needles length neither for CIO (Figure 4) nor CWM samples (Figure 5). We hypothesize that this is due to the formation of the most of

CuO layer in the first 5 minutes of the process. Alkaline solution (2) created smaller feature sizes compared with alkaline solution (1) in all cases. In a subsequent study, the oxidation time was further reduced (1.5 and 3 minutes) in order to form shorter nano needles and avoid closure of the necks in CIOs samples. As shown in Figure 6, oxidation duration of 1.5 minutes using either of the alkaline solutions or oxidation duration of 3 minutes using alkaline solution (2) are fairly effective for the creation of nano needles with a length of less than 100 nm and preventing closure of the pores (diameter of ~5 μm) and necks (diameter of ~1 μm) in CIO samples. The recipe can be further optimized for creation of oxide layers with even smaller thicknesses (Figure 7).

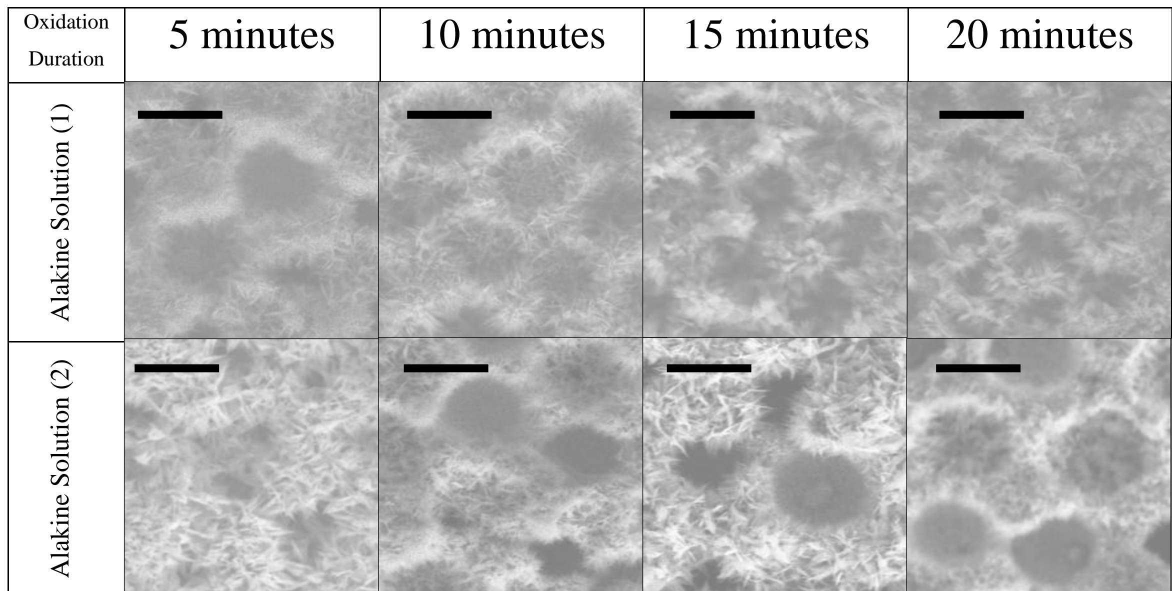

Figure 4. Chemical Oxidation of CIO samples: no significant difference in the morphology of the CuO structure was observed for oxidation duration of 5, 10, 15, and 20 minutes with the chemical oxidation recipe (1) or (2) for CIOs. We hypothesize that this is due to the creation of most of the CuO layer in the first 5 minutes of the oxidation. The CuO layer created in the first 5 minutes prevents further reactions between the copper surface and the oxygen molecules in the solution. Consequently, the growth of the oxide layer slows down significantly after 5 minutes of oxidation. Similar to a previous study [11], we observe that alkaline solution (2) creates smaller nano structures and keeps the necks partially open. This method seems to be promising for the further optimization of the recipe to avoid neck closure. Scale bars are equivalent to 5 μm in all of the images.

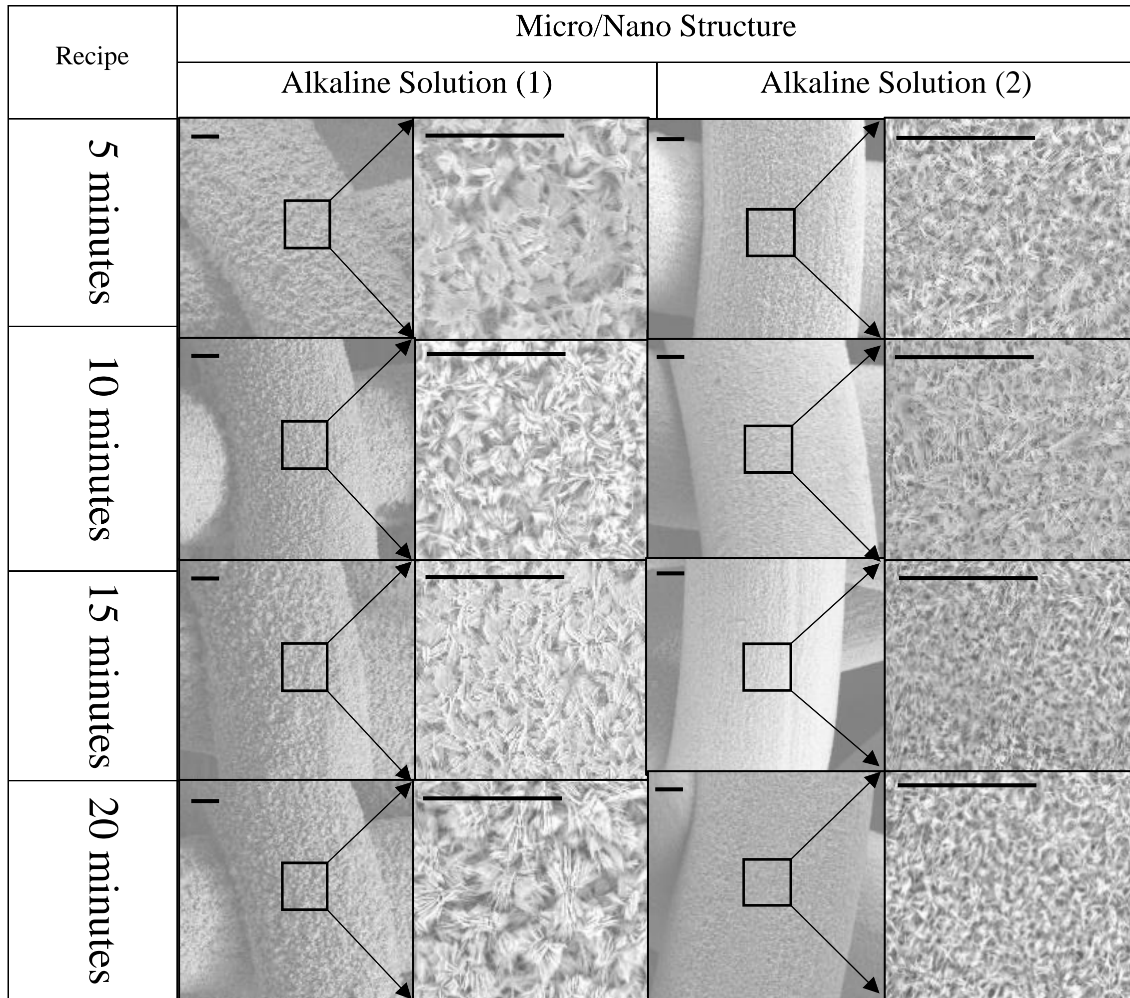

Figure 5. Chemical Oxidation of CWM samples: no significant difference in the overall morphology of the CuO structure was observed for oxidation duration of 5, 10, 15, and 20 minutes in the chemical oxidation recipe (1) or (2) for CWMs. We attribute this to the creation of most of the CuO layer in the first 5 minutes of the oxidation. The CuO "nano flowers" [9] created using alkaline solution (1) have a length of between 2 to 5 μm. The CuO "nano grass" [9] structures created using alkaline solution (2) has a length of between 500 nm to 2 μm. Scale bars are equivalent to 10 μm in all images.

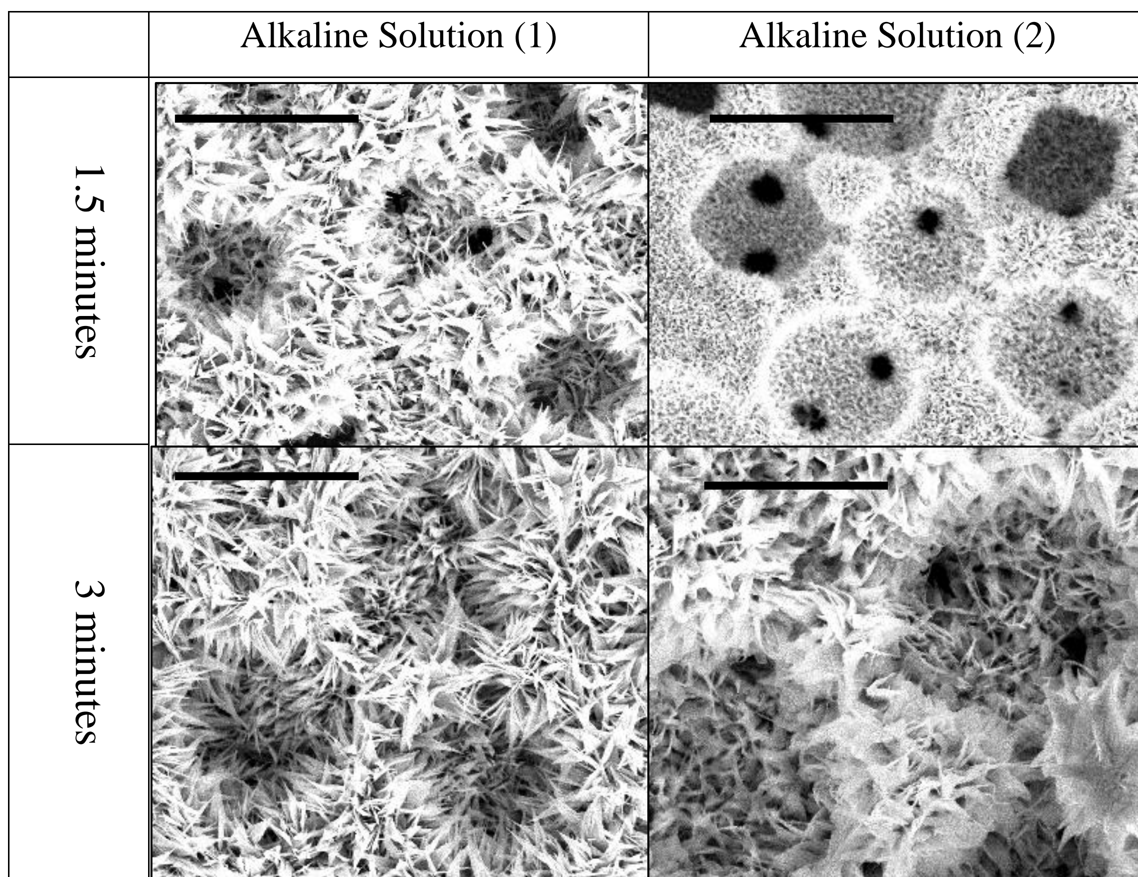

Figure 6. Fine-tuning of the recipe for CIO samples: oxidation duration of 1.5 and 3 minutes with alkaline solution (2) and oxidation duration of 1.5 minutes with alkaline solution (1) does not cause closure of the necks. The nano needles created using alkaline solution (2) for 1.5 minutes have a length of less than 100 nm. Scale bars are equivalent to 5 μm in all images.

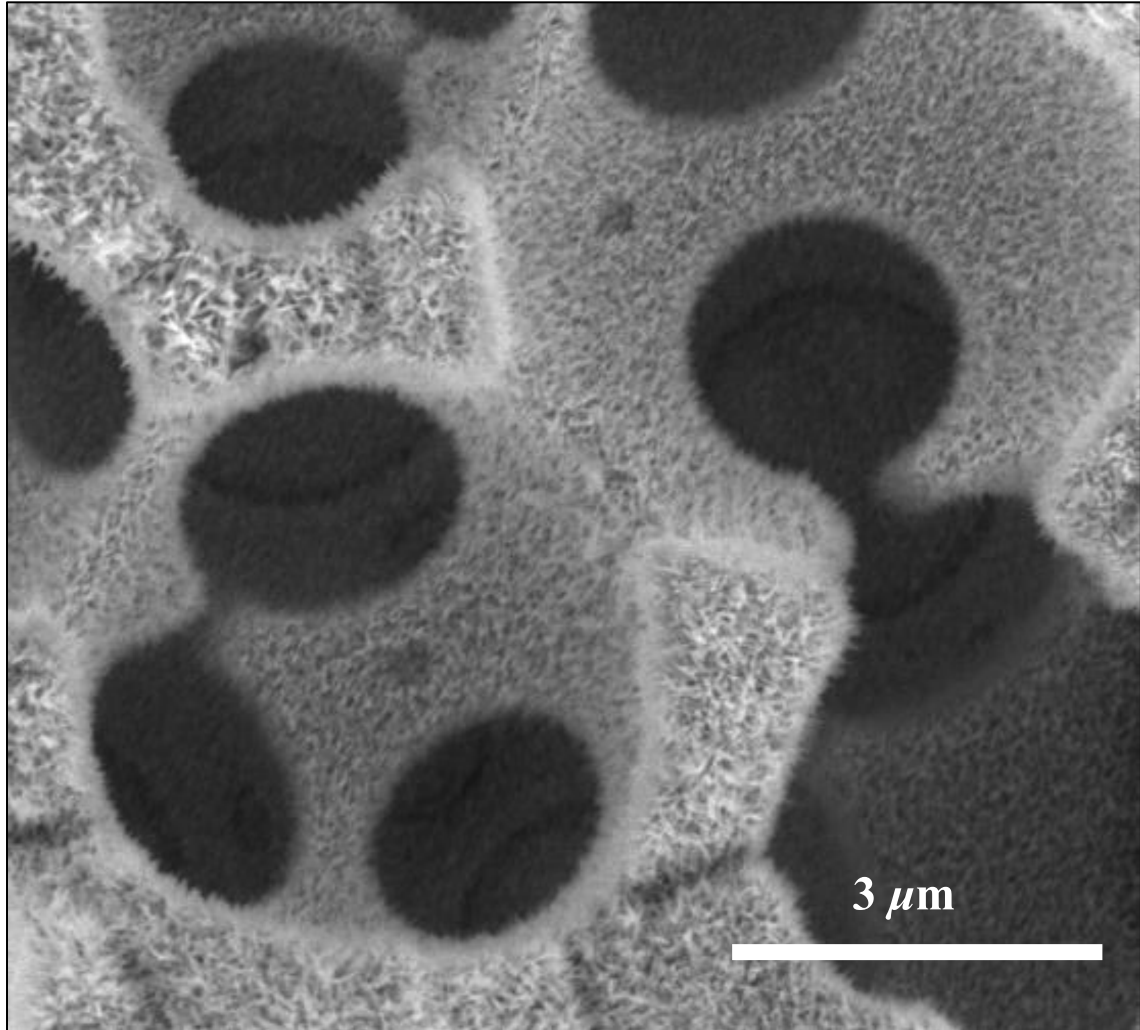

Figure 7. Ultra-short nano grass can be formed over the microporous copper surface by using 1.5 minutes of oxidation in alkaline solution (2) with 50% dilution. Even though this oxide structure seems to be ideal for the capillary-fed boiling application, repeatability of fabrication process of the CuO layer at these small thicknesses seems to be challenging for samples with large area (5×5 mm^2 or more).

2.4. Long-term operation

The resulting CuO nanostructures have minimal impact on the underlying CIOs and successfully create a superhydrophilic structure without deforming or inhibiting any of the fluid flow pathways. As a next step, we characterized the stability of the structure in both ambient heating as well as boiling (Table 3) using a goniometer to measure the contact angle (Figure 8). In addition to exploring whether the structure mechanically survives boiling processes, we also aim to explore if the hydrophilic nature of the structure is preserved as well. Previous studies [1-10] concluded that CuO films may transition from superhydrophilic to hydrophobic, though the majority of the experiments were done in ambient conditions with varied reasoning behind the wettability transition such as decomposition or contamination. While one hypothesis is that the partial surface-level deoxidation of CuO back into Cu_2O may result in the contact angle change [4, 7, 10], other studies attributed the wettability transition in CuO films to adsorption of surface organics [8]. It remains inconclusive whether partial deoxidation of the CuO nanostructures back into hydrophobic Cu_2O should be a reason for concern, or if it is irrelevant to the evaporator wick application. Therefore, we characterize the stability of the CuO coating that we formed over the CIO structure in the operating conditions, such as immersion in boiling water, appropriate for the evaporator wick.

As seen in Figure 9, the initial hydrophilic contact angle changed to hydrophobic after heating in the room environment, however; hydrophilicity of the surface is reversible using a cleaning protocol. After submerging of the samples in consecutive Acetone, IPA and water baths (10 minutes each) the surface became superhydrophilic. Acetone was used to remove the organic

contaminants; IPA was used to remove Acetone residues and water was used to remove IPA. Effectiveness of Acetone in changing the contact angle of the surface confirms the previous observation in O_2 treatment (Figure 1) and hypothesis of the previous studies [8] regarding the role of the organic contaminants in creation of a hydrophobic surface on copper. While the current study suggests that boiling experiments does not affect hydrophilicity of the structure (Figure 9), the proposed cleaning protocol can be implemented in situations which a hydrophobic contact angle was observed for the generated CuO layer during the long-term device operation.

Table 3. Various conditions, time, temperatures and contact materials for the contact angle measurements

Condition	Time	Temperature	Contact
1	After oxidation	25 C	Room (ambient)
2	>12 hours	100 C	Oven (ambient)
3	>6 hours	25 C	Room (ambient)
4	3sec, 3X	25 C	Water rinse, Air Gun Dry
5	10min, 3X	25 C	Acetone, IPA, Water Bath
6	>12 hours, 4X	100 C	Boiling Chamber (water)

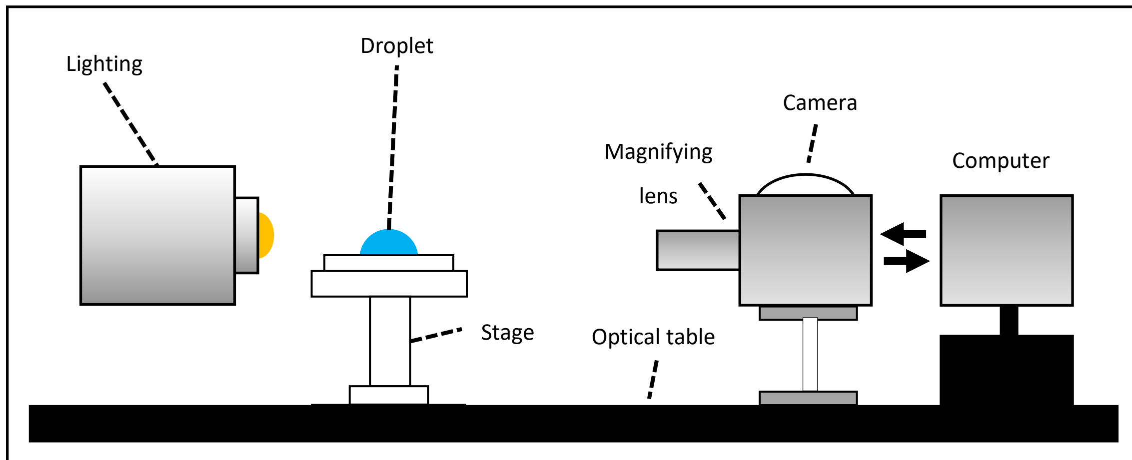

Figure 8. Contact angle measurement setup: Goniometer Rame-Hart 290 and an image processing software were used for droplet control, imaging, and contact angle measurement.

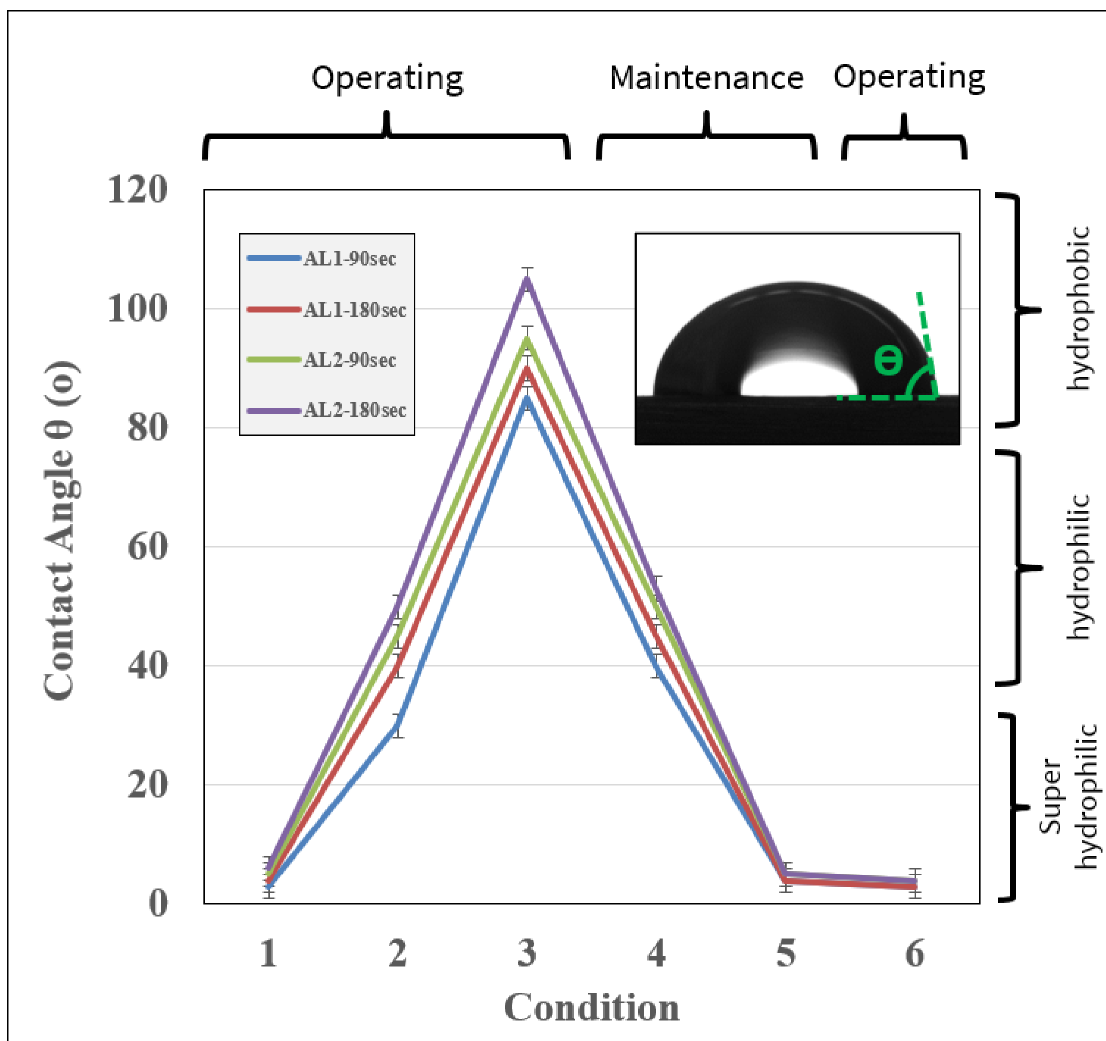

Figure 9. Contact angle measurement of copper inverse opal (CIO) structure in various operating and maintenance condition for 4 different chemical oxide formulas. All of the CIO samples have superhydrophilic contact angle after oxidation, however; the surface became hydrophobic for all of the cases after >12 hours of heating at > 100 ^{o}C followed by ~6 hours in the room environment at ~25 ^{o}C. Water rinsing and air drying was effective for creating a hydrophilic contact angle for the samples that were oxidized using alkaline solution 1. We hypothesized that hydrophobicity is due the organic contaminants and used consecutive baths of Acetone, IPA, and water to decreases the contact angle. Superhydrophilic contact angle after the cleaning process was stable even after 48 hours of boiling test.

Chapter 3

Fabrication and Characterization of Evaporator

Phase change thermal management devices including heat pipes and ultra-thin vapor chambers can remove and spread the excess heat from microprocessors more efficiently compared with the conventional heat sinks. However, the capillary and CHF limits of the evaporator section remained a challenge for high heat flux and large area applications. In this study, a hybrid microporous structure consists of copper wire meshes (CWMs) as the liquid delivery routing and copper inverse opals (CIOs) film as the boiling/evaporation platform is proposed. The microporous wick is fabricated using copper electrodeposition and then tested in a boiling chamber at saturated environment (liquid water and vapor at ~100 ^{o}C). The hybrid microporous structure was able to remove 153.3 W from the 5×5 mm^2 heater area (613.2 W cm^{-2} heat flux) with 13.1 ^{o}C super heat resulting in thermal resistance of 0.02 cm^{2o}CW^{-1} at the CHF. Large portions of this chapter are taken from Soroush et al., "A Hybrid Microporous Copper Structure for High Performance Capillary-driven Liquid Film Boiling", ASME 2021 International Technical Conference and Exhibition on Packaging and Integration of Electronic and Photonic Microsystems, 2021.

3.1. Evaporator fabrication

3.1.1. Fabrication of copper wire mesh (CWM) wick

Before fabrication of the hybrid wicking structure, we fabricated and tested wire mesh **only** wicking samples for direct comparison with results from Wen et al. [17]; this will serve as a baseline for comparison with the CWM-CIO hybrid wicking structure. The fabrication process for single layer wire mesh is outlined in Figure 10.

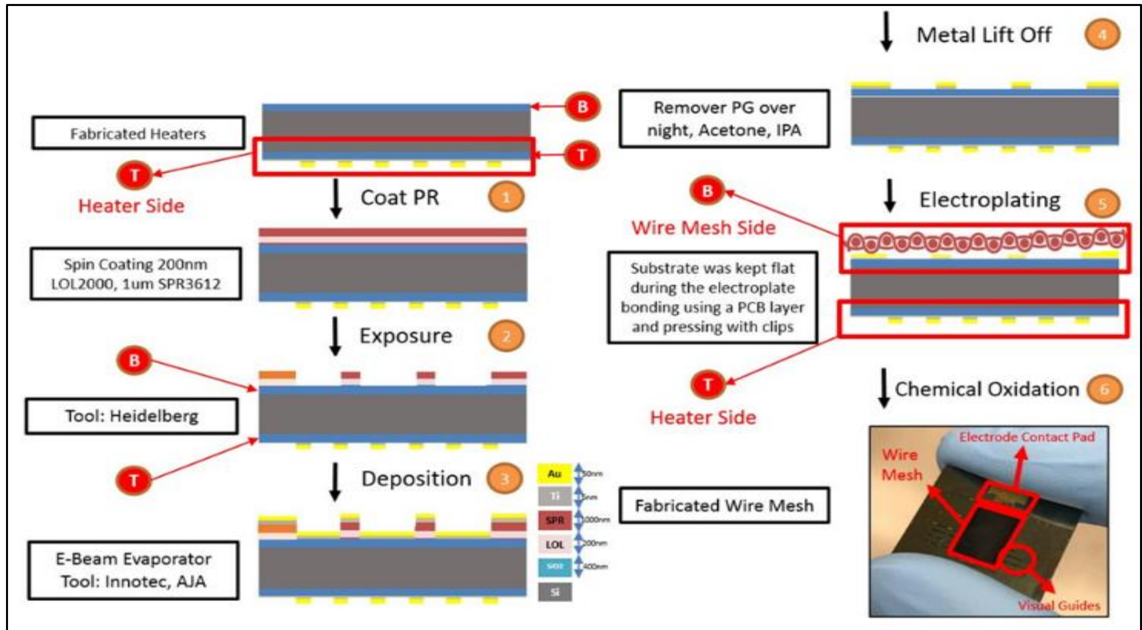

Figure 10. The fabrication process of Single layer wire mesh without CIOs: after fabrication of heater and RTDs on top **(T)** side of the silicon substrate, **(1)** the bottom **(B)** side of the silicon substrate is spin coated with 200 nm of LOL2000 and 1 μm of SPR3612. It is vital in this step to protect the heater on the top **(T)** side with adhesive to avoid damage to the RTDs. In the next step **(2)**, the resist is exposed using a mask less UV laser to define the seed layer for electroplating the CIOs. Subsequently, **(3)** 10 nm of Ti and 100 nm of Au are evaporated over the bottom (B) side of the Silicon chip. Next, **(4)** the wafer was left in Remover PG over 12 hours and then, sonicated in acetone bath for 5 minutes and rinsed with IPA and water. At the end, wafers are dried in SRD (Spin-Rinse-Drier) machine for 10 minutes and diced into 18×22 mm^2 chips. Afterward, (**5)** A single layer copper wire mesh is electroplate-bonded to the Titanium-Gold seed layer. Finally, **(6)** A chemical oxidation formula (see Chapter 2) is used to maintain the hydrophilicity of the surface.

3.1.2. Fabrication of copper inverse opals (CIOs) on large areas

The fabrication process of the CIO structure is outlined in Figure 11. The resulting microporous structure is shown in Figure 12. For thermal tests of the CIO+CWM structure, tile openings are made using laser cutting and then the wire mesh was placed on top of the CIO structure. Although freshly fabricated copper is inherently hydrophilic, the wettability of the surface reduces quickly due to surface absorption of organic contaminants and the formation of a cuprous oxide layer (Cu_2O). To maintain the wettability of the surface, samples are pre-oxidized using a chemical surface treatment (see Chapter 2) before the boiling tests to form a stable hydrophilic cupric oxide layer (CuO).

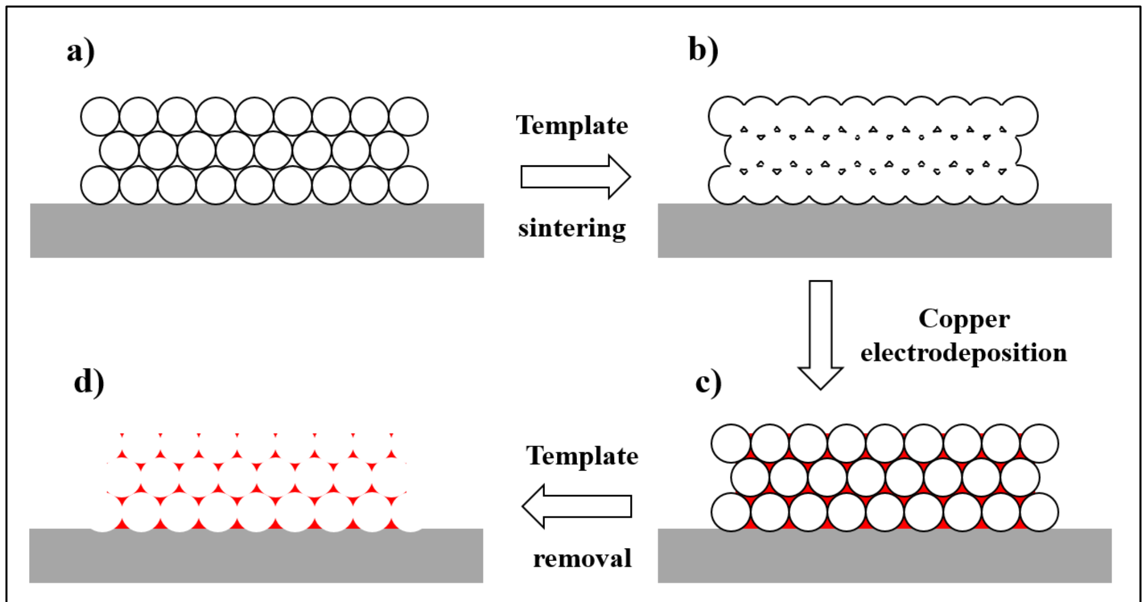

Figure 11. Schematic of the fabrication process of the micro porous copper using sacrificial template. **(a)** Polystyrene spheres are self-assembled into an opal template, creating point contacts between adjacent spheres. **(b)** Necks between adjacent spheres are formed during the sintering process by template densification. **(c)** Electrodeposition of copper and growth of the micro porous structure around polystyrene templates. **(d)** Removal of sacrificial template using solvent results in the copper inverse opal structure.

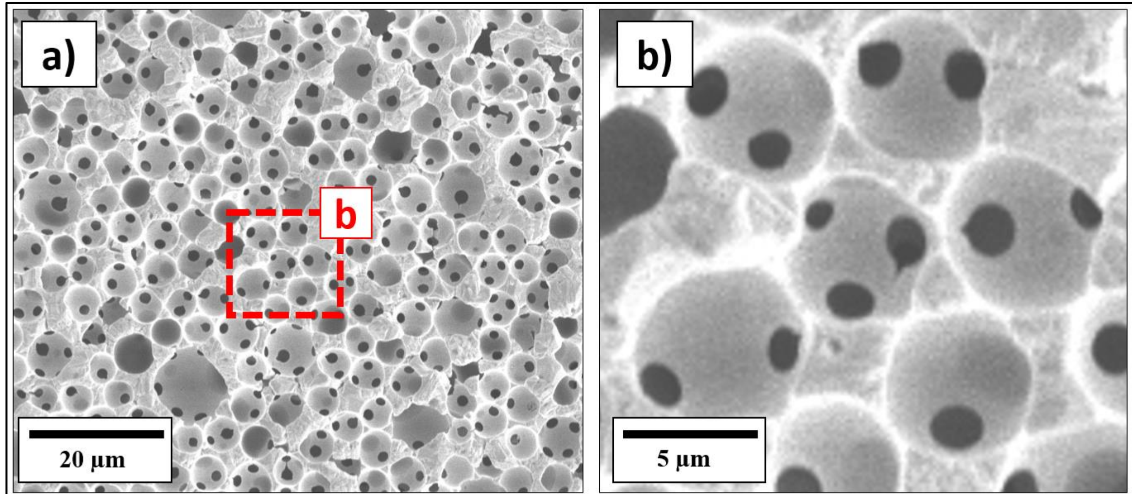

Figure 12. (a) Top view of the micro porous copper structure under scanning electron microscopy. **(b)** Pores and fluid permeable interconnects or 'necks'.

3.1.3. Fabrication of hybrid microporous structure

The fabrication process of the hybrid structure is outlined in Figure 13. The resulting hybrid microporous structure (high quality) is shown in Figure 14. While the hybrid structures shown in Figure 14 have the desired quality, the repeatability of the fabrication process for these samples is not high (especially during the electroplating step) and has several challenges (Figure 15). We developed methods and recipes to circumvent some of issues (Figure 16, 17); however, significant amount of work needs to be done in future studies in terms of the fabrication yield and time in order to use these structures for industrial applications.

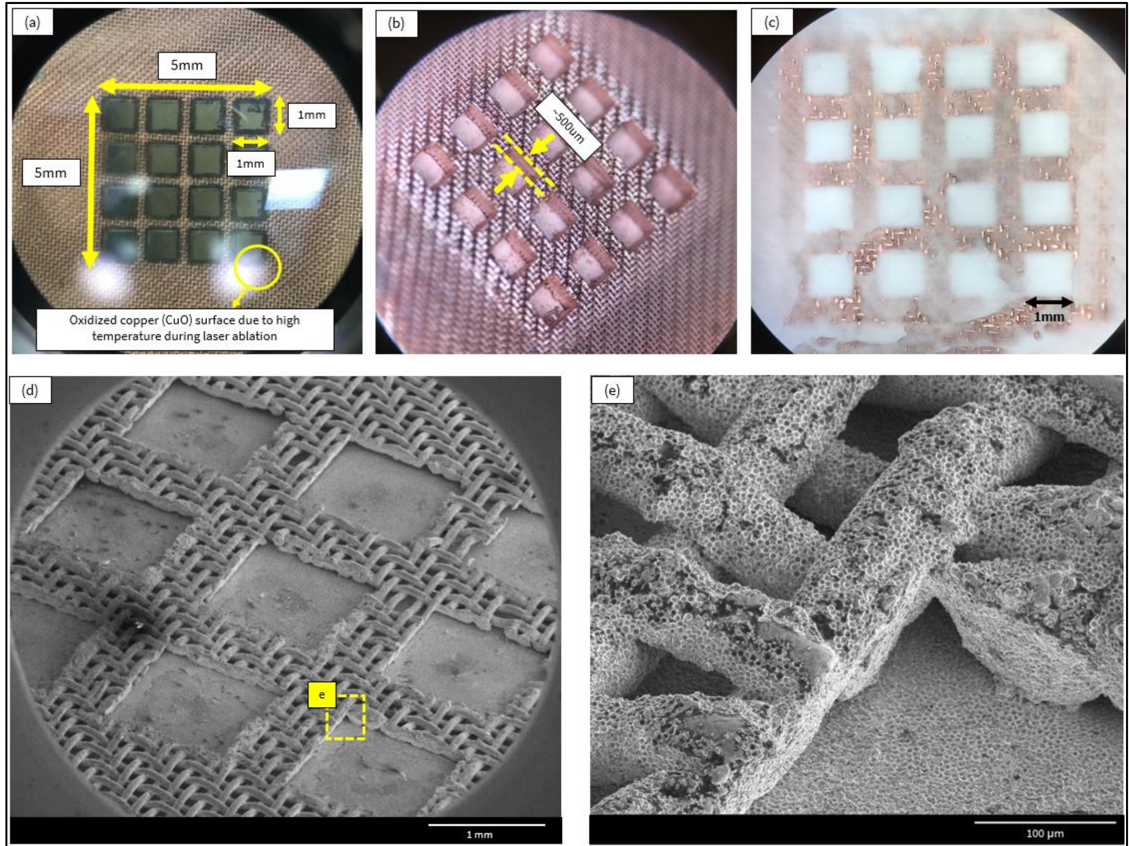

Figure 13. Fabrication process of the hybrid microporous structure: **(a)** Laser cutting of the copper wire mesh. **(b)** Electroplate-bonding of the copper wire mesh to the titanium-gold seed layer. **(c)** Filling the tiles with the polystyrene spheres and swiping a blade for better packing (doctor-blading) **(d-e)** Electroplating copper and dissolving the spheres.

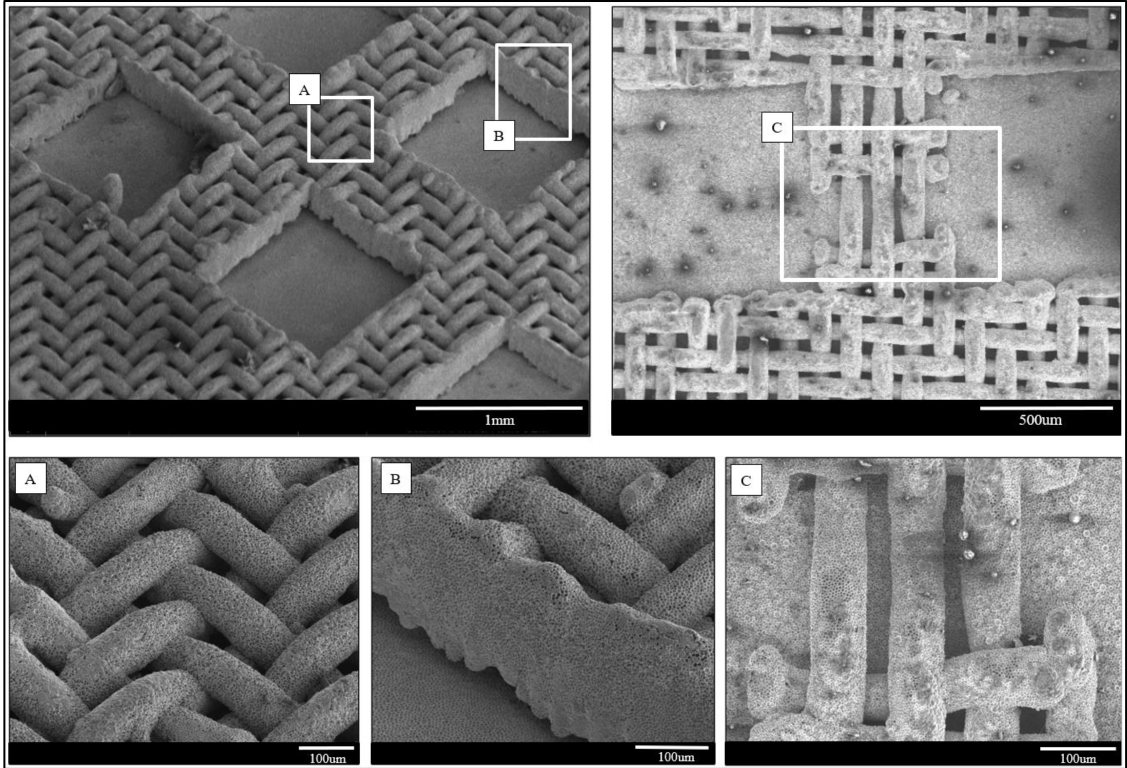

Figure 14. High quality hybrid microporous wicks: (**a**) conformal coating of CIOs on wires. (**b**) conformal coating up to 100 μm depth. (**c**) CIOs coverage under the wires.

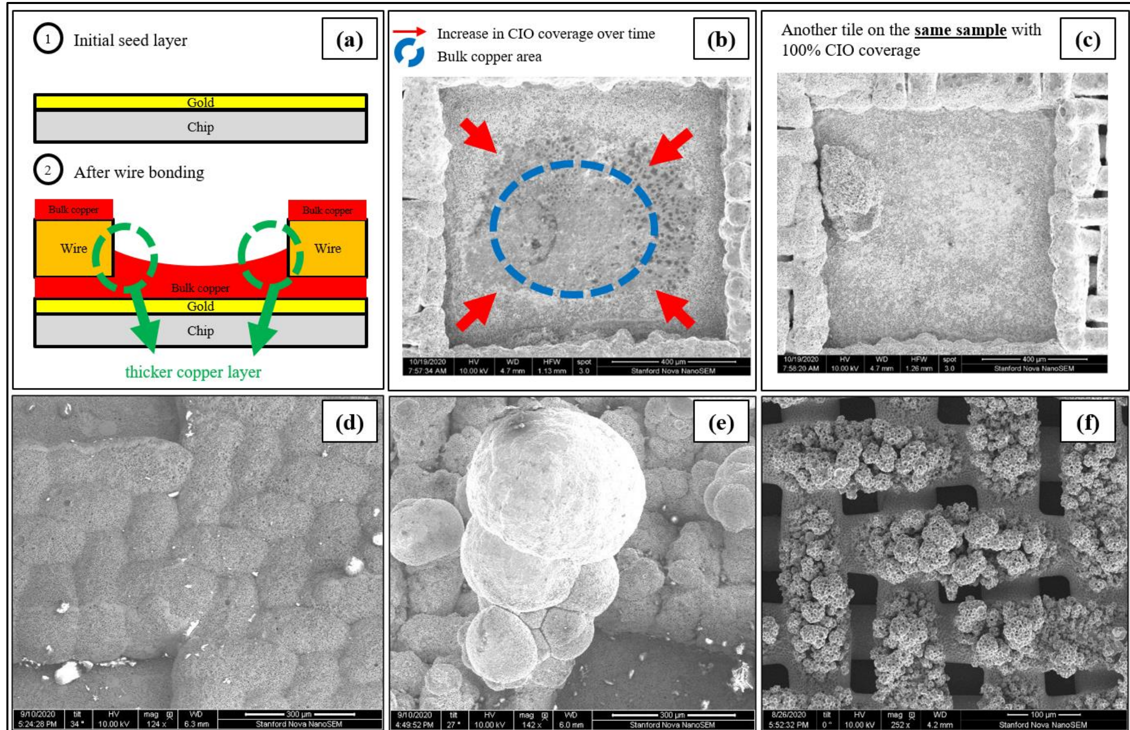

Figure 15. Fabrication challenges of hybrid microporous wick: **(a)** Non-uniformity of CIOs thickness in each tile. **(b-c)** Variation in CIOs thickness over the tiles of the same sample. **(d)** Full pore closure of the copper wire mesh. **(e)** Formation of bulk copper bumps. **(f)** Non-uniformity in CIOs coating on copper wires.

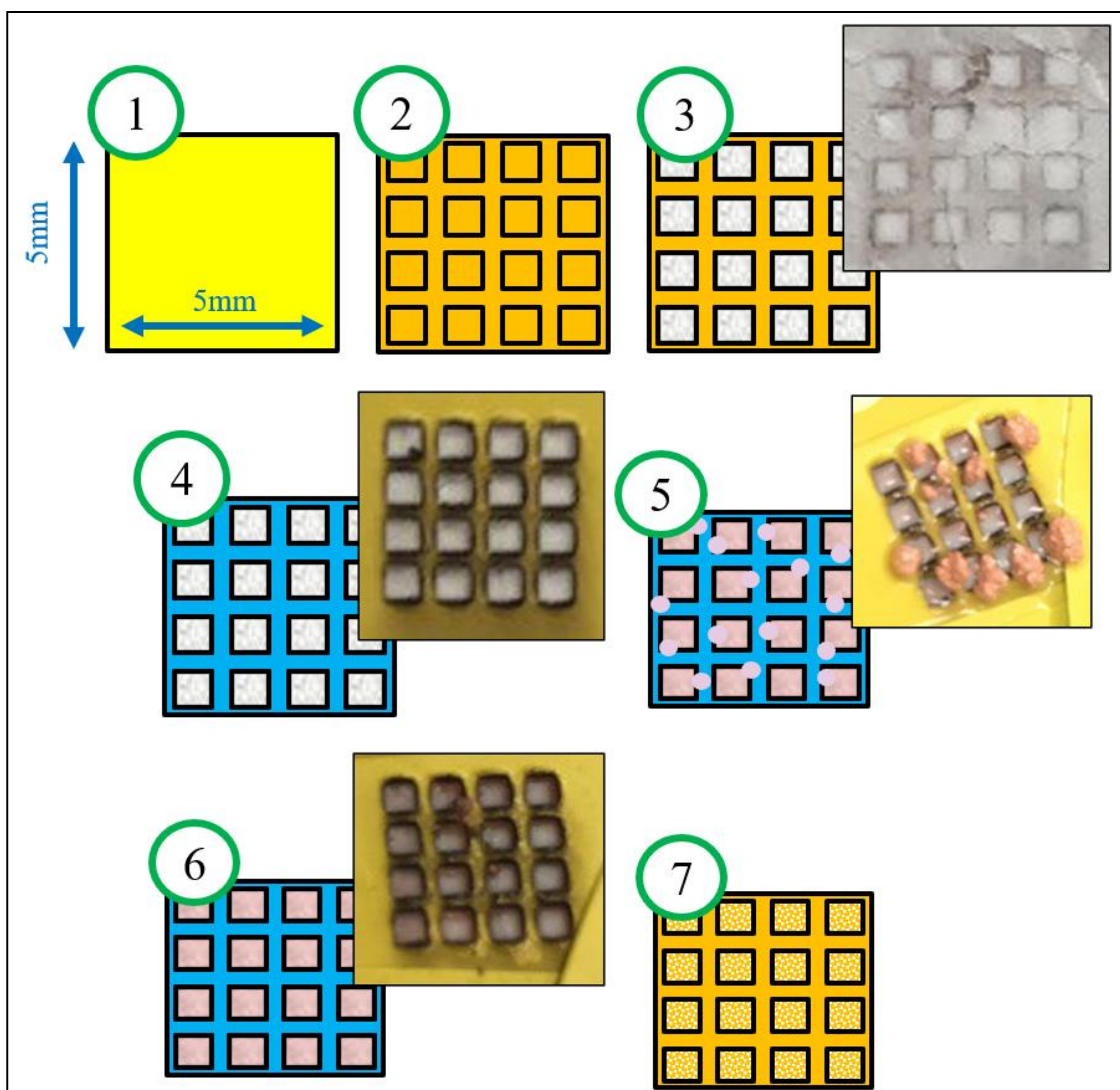

Figure 16. Refined fabrication process to remove the bulk copper bumps: (1) Deposition of 10 nm titanium and 100 nm gold. (2) Electroplate-bonding of the copper wire mesh. (3) Doctor-blading of polystyrene spheres. (4) Laser cutting and bonding of a single layer acid resist tape. (5) Electrodeposition of inverse opals. (6) Removal of the bulk copper bumps with a razor blade without damaging the wire mesh structure. (7) Dissolving the template using organic solvents.

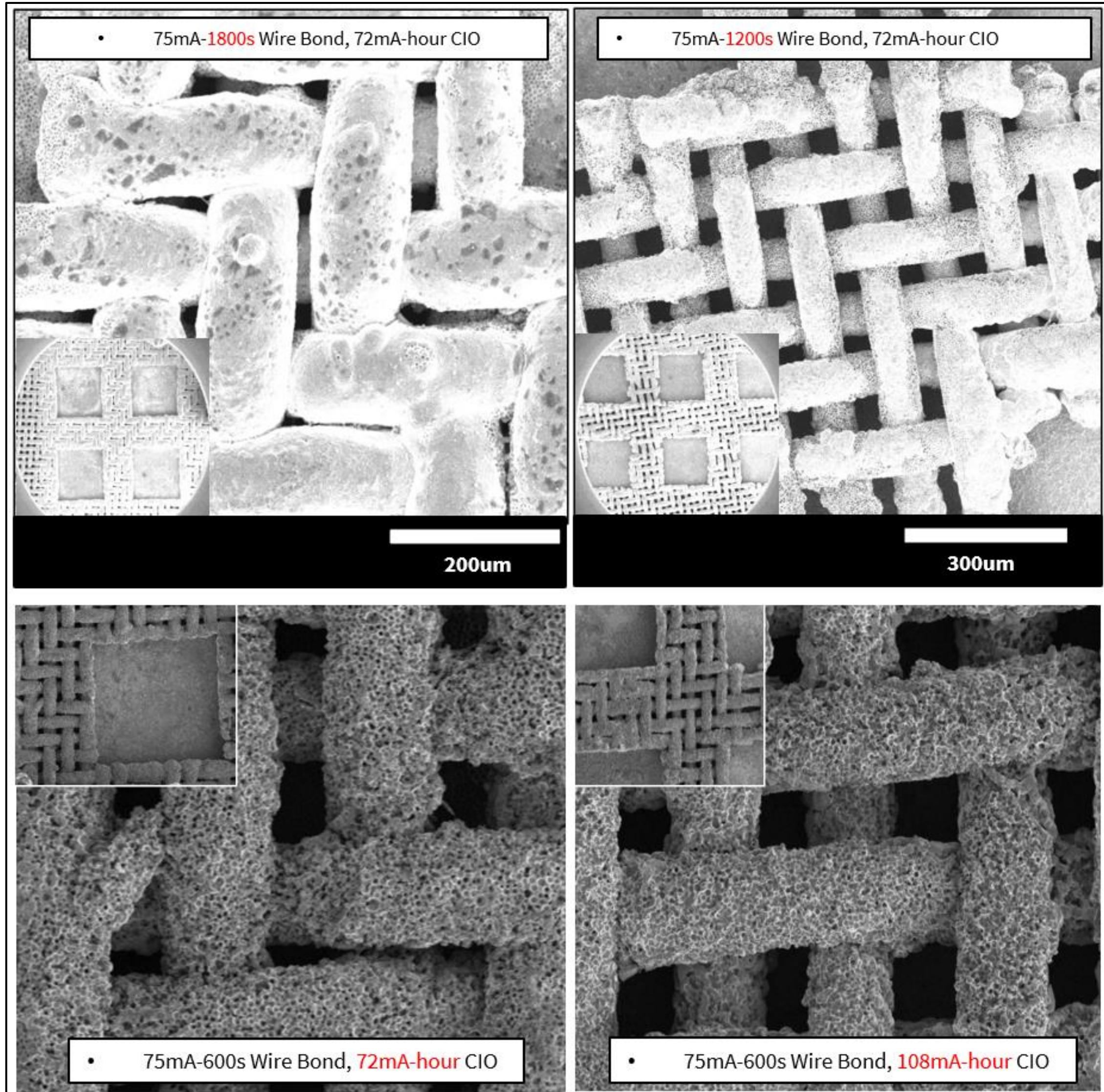

Figure 17. Refined fabrication process to prevent pore closure in copper wire mesh (CWM): (Top) Early fabrication steps resulting in pore closure in wires due to the over plating of copper during the wire bonding process. (Bottom) Reducing the electrodeposition time to 600 seconds during wire bonding prevents the pore closure regardless of the CIOs electroplating step.

3.2. Evaporator characterization

3.2.1. Experiment Setup

A flow loop and a vapor chamber are designed and fabricated to provide a saturated environment with liquid level control in capillary-fed boiling experiments (Figure 18(a-c)). Temperature measurement and power supply have been done using RTDs, a serpentine heater, and pogo pins on the backside of the Silicon chips (Figure 18d). The calibration process for RTDs was done for each sample before thermal tests (see Appendix). For each experiment, at least 3 hours of rigorous boiling was done as a degassing process to evacuate the air inside of the flow loop and create a saturated environment. The water level is controlled inside of the chamber with 1 mm precision to keep the meniscus level below the $5{\times}5$ mm^2 hot spot area and maintain liquid feeding as a capillary regime. Since capillary wicking occurs against gravity, no flooding over the wicking structure will occur. For each heat flux, at least 5 minutes of steady state condition both for temperature readings and liquid feeding is maintained, and then, superheat temperature (average value of the five RTDs embedded in the serpentine heater) is reported.

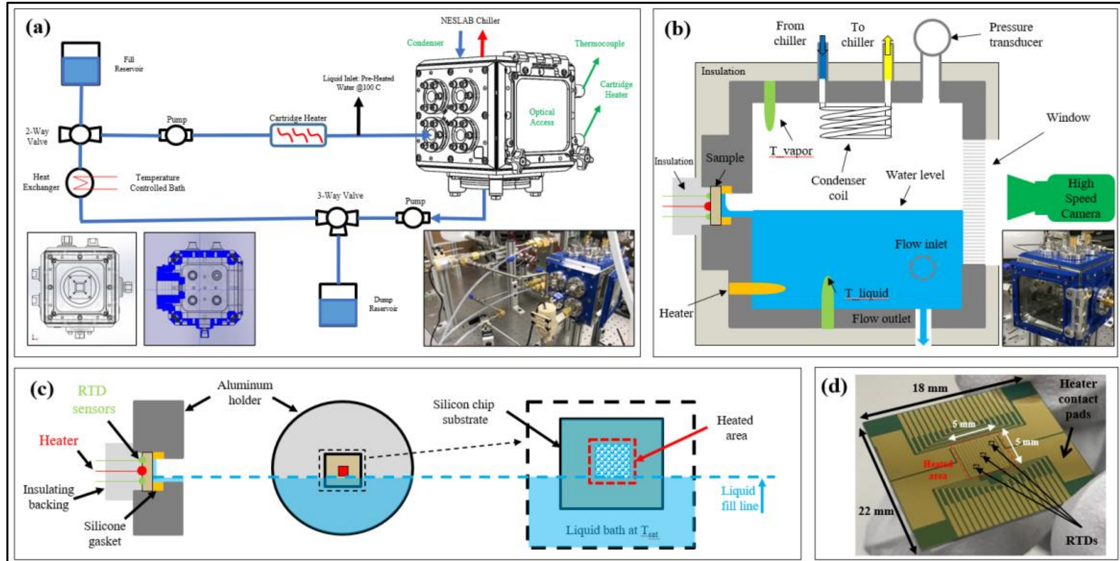

Figure 18. (a) Schematic of the flow loop: In order to have better control on the liquid level and meniscus area, preheated water at the temperature of >98 °C is fed to the vapor chamber and heated up to 100 °C inside the chamber using a cartridge heater. This procedure significantly reduces bubble generation and water level fluctuations inside of

the chamber and provides a very stable meniscus. Due to the high rate of evaporation from the flow loop and inside the chamber, the condenser coil and NESLAB chiller help with maintaining the liquid level with 1 mm precision during 6-8 hours of boiling tests. Liquid water was circulated at temperature of 85 ^{o}C to provide the required condensation along with minimal impact over the heat loss. All pipes and connections in the flow loop were covered with 10 cm foam for better isolation. **(b)** Wicking structure inside of the vapor chamber: Liquid level and the meniscus are controlled to be below the hot spot area during the boiling tests to retain a capillary-fed boiling regime. **(c-d)** Up to 5 RTDs with 2 μm tip width are placed inside of the heater serpentine. The average of the 5 recordings is reported as the superheat temperature. Pogo pins are used to supply power to the serpentine heater. A PCB configuration is designed and fabricated to connect RTD pads on the silicon chip to the electrical wires. The temperatures are measured using the 4-wire measurement method.

3.2.2. Thermal tests

Thermal performance for the single layer CWMs sample without CIOs (see section 3.1.1) was very similar to the results reported by Wen et al. [17]. CHF of the sample was ~28 Wcm^{-2} at superheat temperature of 8 ^oC (thermal resistance of ~0.3 $cm^{2o}CW^{-1}$) (Figure 19 (Top)). On the other hand, the thermal performance was increased significantly by combining CWMs with CIOs. The CHF reported by Wen et al. [17] for 5-layer diffusion bonded copper wire mesh was less than 150 Wcm^{-2}, while the wick structure combining CWMs with CIOs (without perfect bonding of the wire mesh to the seed layer, see section 3.1.2) was able to reach CHF of ~300 Wcm^{-2} (Figure 19 (Middle)) with ~9 ^oC superheat (thermal resistance of 0.03 $cm^{2o}CW^{-1}$ at the CHF). The sample was super hydrophilic after the thermal tests and the CIO structure was not deformed, showing promise for the feasibility of implementations in the device level (i.e. Silicon-based UTVCs) and the industrial applications. The hybrid micro porous structure was able to provide high thermal performance and modeling results predict a higher heat flux of ~600 Wcm^{-2} at <20 ^oC superheat. The lower heat flux in the experiments is due to an early dryout region and the low thermal conductivity of the CWMs in this configuration. The gaps between the CWMs and the CIOs in the center of the hot spot area results in a micro scale separation and restriction in the liquid delivery (Figure 20). Consequently, there will be a sudden increase (<10 seconds) in the local temperature (>500 ^oC) and burning out of the heater serpentine. Moreover, an air gap between the wires can reduce the thermal conductivity of CWMs down to 0.1 $Wm^{-1}K^{-1}$ (compared with 100 $Wm^{-1}K^{-1}$ in the direct contact condition) [18].

In the next step, we tested the hybrid structure discussed in section 3.1.3. As shown in Figure 19 (Bottom), heat flux of 613.2 W cm^{-2} with 13.1 ^oC super heat was achieved using this structure, showing 15 times improvement in the thermal resistance of the structure compared with the simple CWM. The better contact between the wires and the seed layer results in a significant increase in the thermal performance of the CWMs and prevents the early dryout in the CIOs regions. Increasing the neck to pore ratio in the CIO structure increases the permeability and reduces the thermal resistance.

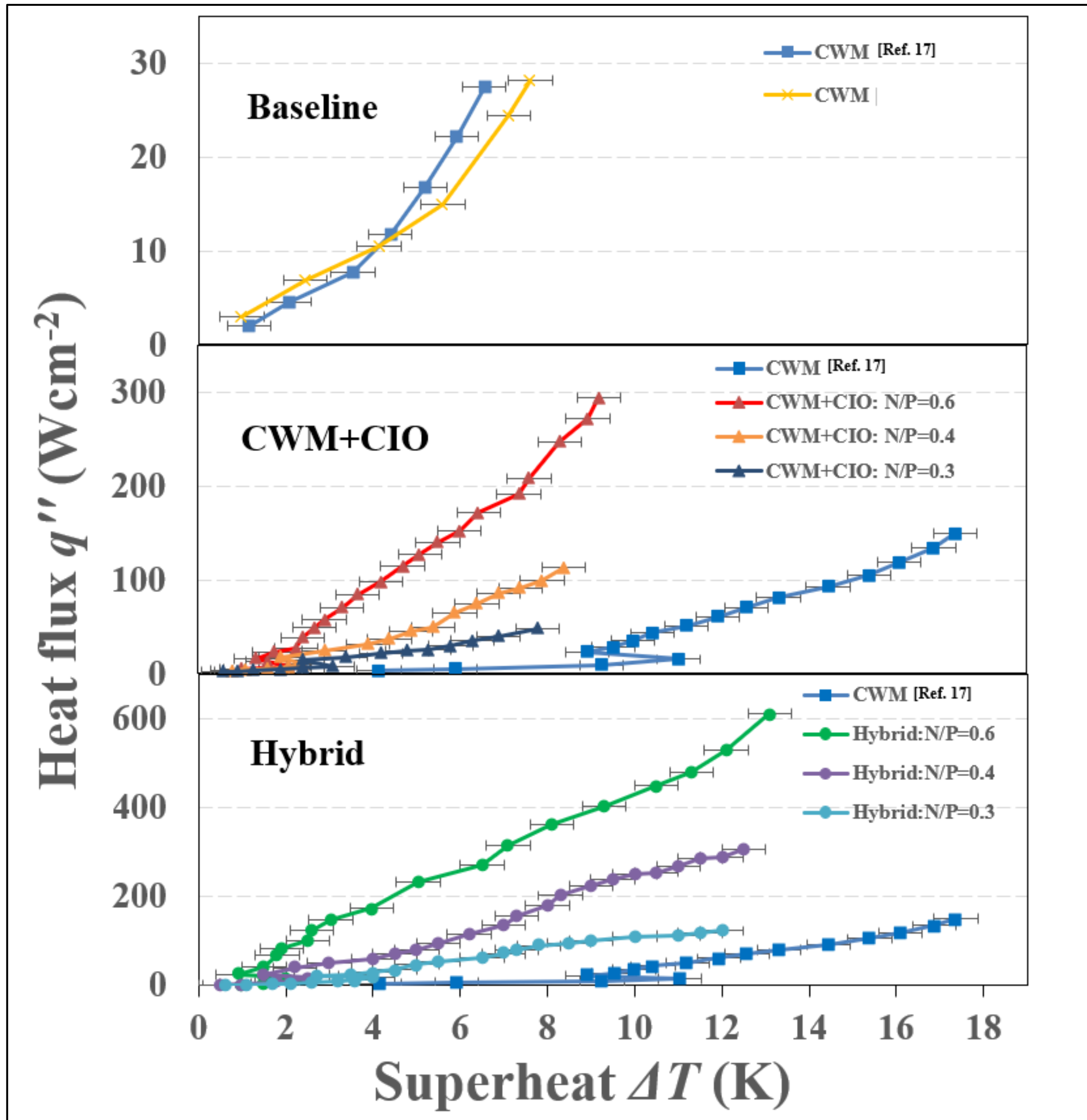

Figure 19. Significant enhancement in thermal performance by incorporating microporous copper in the wire mesh wicking structure: heat flux (*q''*) is plotted as a function of superheat (*ΔT*). Onset of boiling occurs in the hybrid structure earlier than the simple CWM structure. This is due to the fact that the smaller pores in CIOs (5 μm) significantly help with the creation of the bubble nucleation sites in the beginning of the boiling process.

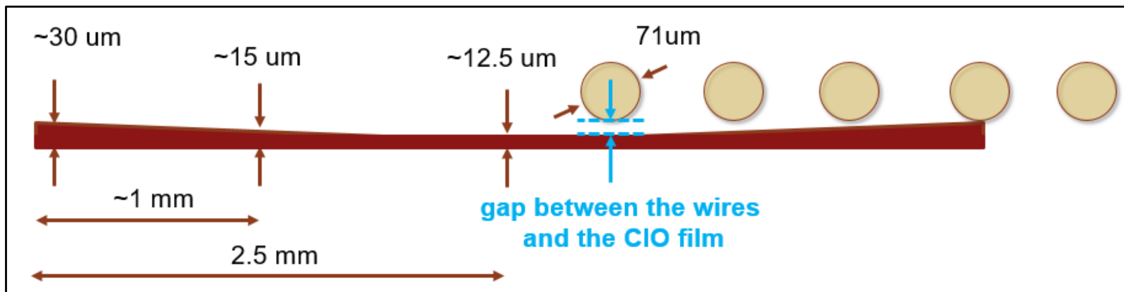

Figure 20. Schematic of CIO+CWM structure: variation in the thickness of the CIOs film (12.5 μm – 30 μm) along with implementation of the mechanical fixtures on the sides of the chip to hold the CWM on top of the CIOs results in an unreliable contact in the central regions of the hotspot. The lack of the proper bonding during the boiling causes the low liquid feeding at high heat fluxes and the occurrence of the early dryout regions.

Chapter 4

Vapor Chamber Design and Reliability

Thermo-fluidic performance of ultra-thin vapor chambers has been studied extensively in the past two decades, however; the thermo-mechanical design and reliability of these devices has not received much attention. For the operating condition at >150 ^{o}C with water as the working fluid, the device must withstand the vapor saturation pressure of ~0.5 MPa. The mechanical design and reliability of the vapor chamber is therefore crucial for avoiding the device breakdown or leakage due to the high internal pressure. In this study, we develop a parametric model for thermo-mechanical design and structural analysis of an ultra-thin (1 mm thickness) miniature (15×15 mm^2 area) silicon vapor chamber. We study the effects of various design parameters such as cavity area, cavity thickness, and fillet radius. For the first time, we introduce the circular cavity design for the vapor chamber application. To increase the mechanical reliability, we propose the implementation and study the design parameters of various mechanical support structures such as ribs, crossbars, and micro-post arrays. The critical point of the mechanical design is the evaporator-condenser bonding area. Gold-tin and gold-silicon eutectic bonding are proposed as the bonding materials and methods. The samples and the tensile test setup are designed and fabricated specifically for the vapor chamber application. Large portions of this chapter are taken from Soroush et al., "Mechanical Design and Reliability of Gold-Tin Eutectic Bonding for Silicon-based Thermal Management Devices", IEEE Intersociety Conference on Thermal and Thermomechanical Phenomena in Electronic Systems (ITherm), IEEE, 2020

4.1. Thermomechanical model

A simple schematic of the device is demonstrated in Figure 21(a). The ultra-thin vapor chamber is fabricated using two separate substrates (i.e. evaporator and condenser) that are bonded together using permanent bonding methods such as gold-tin or gold-silicon eutectic bond. The working fluid inside of the device is changed into the vapor using an evaporator wick heated by the chip. The vapor raises to the condenser, spreads to the side walls, and the condensed fluid comes back to the evaporator section. Using capillary wicking, the evaporator is fed by the liquid, and the cycle repeats. The cross-section

schematic also shows an approximation of the mechanical boundary conditions in the chamber. Here we assumed a reliable bonding between the evaporator and the chip, resulting in a fixed plane with zero displacements in all directions. The pressure induced by the vapor is applied to the condenser and the sidewalls, resulting in a bending moment in the corner of the cavity (Figure 21(b)). As shown in Figure 21(c), the bending moment can cause tensile stresses up to 20 MPa in the corner of the condenser for the operating temperatures of as low as 110 ºC. In the present study, we implement various design approached to reduce this bending moment. A few design guidelines emerge from Figure 21(a-c). The effective length of the cavity L_{core} is the main parameter that increases the bending moment and should be reduced for improving the safety factor. Reduction in the cavity thickness t_{core} will also be helpful for decreasing the stress. Additionally, a larger fillet radius rf will effectively reduce the stress in the corner of the device. A circular cavity design might result in a better stress distribution around the edges. Moreover, implementation of micro-post arrays or other support structures might help with deceasing the bending moment.

Regarding the boundary conditions, we assume an isothermal steady-state condition where the temperature of the silicon vapor chamber, the fluid, and the vapor are all equal across the domain. Assuming the vapor to be saturated everywhere, we estimate the vapor pressure based on the temperature using Clausius–Clapeyron equation. Same as [31, 32], the pressure is applied uniformly inside the cavity. Sidewalls and the condenser are free to move in any direction while the evaporator is assumed to be bonded and have zero displacements. This is the worst-case scenario for the mechanical stress analysis since any type of mechanical confinement reduces the bending moment. In each study, only one parameter (e.g. cavity thickness) has been changed and the baseline geometry is constant in all of the designs.

The 3D model of the silicon vapor chamber was generated using SolidWorks and imported into the ANSYS workbench thermal module. Isothermal modeling has been conducted and the result was fed into the ANSYS mechanical module with the mentioned boundary conditions. Mesh independence study has been conducted and simulations has been performed with less than 3% error in the maximum principal stress σ_{max}. The baseline

geometry has been meshed with 3,853,746 nodes, 2,357,988 elements, and adaptive mesh sizing with defeaturing size constant of 0.001.

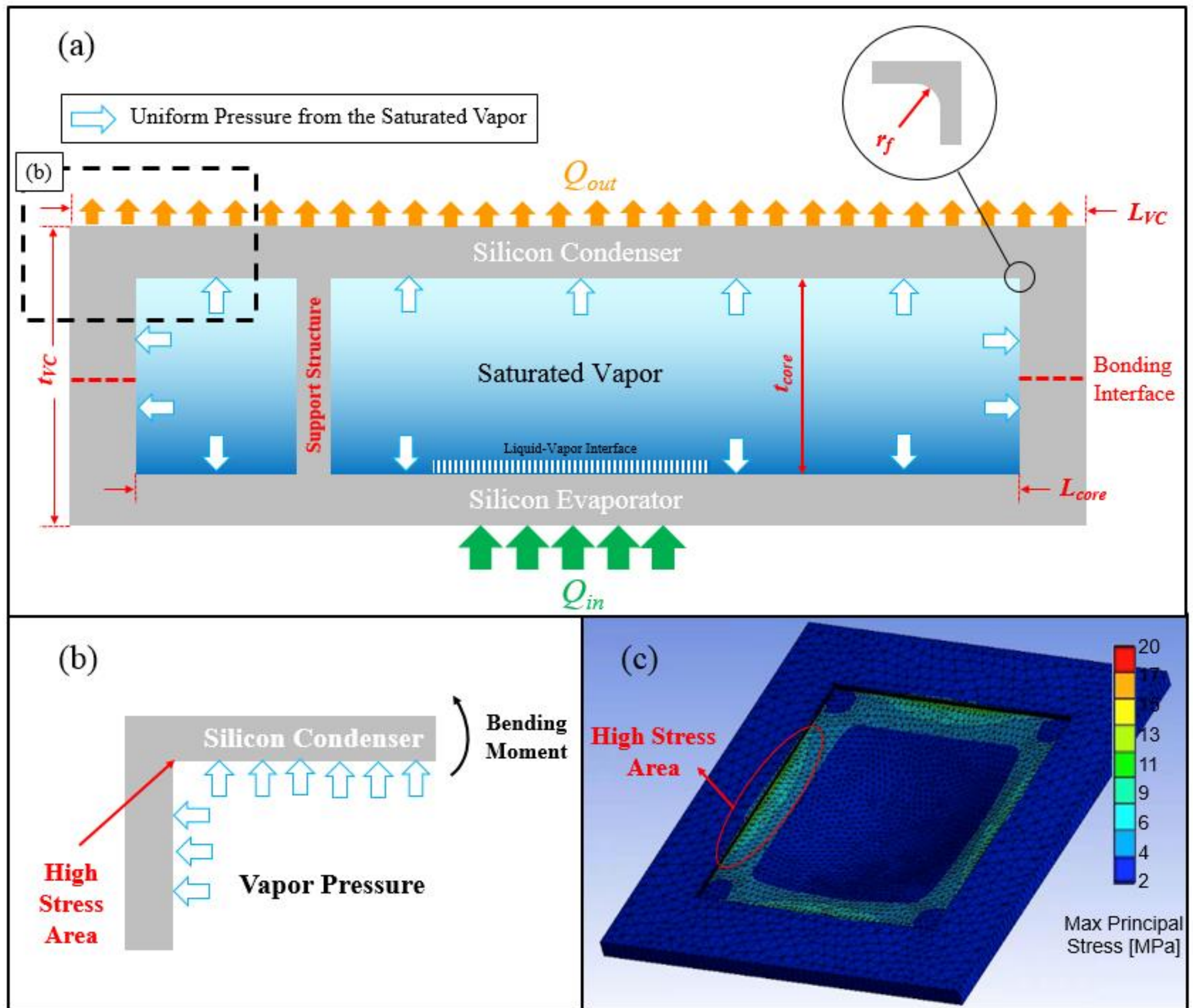

Figure 21. (a) Vapor generation inside the UTVC will result in a significant pressure inside of the cavity that will cause mechanical stresses in different sections. **(b)** A simple schematic shows the bending moment will result in a tensile stress in over the cavity edges in the condenser section. **(c)** A sample simulation result for the baseline cavity design (15×15 mm^2 cavity area, 50 μm cavity edge fillet radius, 400 μm cavity thickness) at the working temperature of 110 ºC shows the maximum principal stress up to 20 MPa (tensile) over the cavity edges.

4.2. Modeling results

Here, we present the results for the parametric geometric study of the vapor chamber. For each design, the maximum stress is calculated based on the simulation model and placed into the following equation for the safety factor

$$Safety\ Factor = \frac{\sigma_{tensile.\ Si}}{\sigma_{max}}$$

where σ_{max} and $\sigma_{tensile,\ Si}$ represent the maximum tensile stress in the design and the fracture strength of silicon, respectively. Simulations have been conducted for temperatures ranging from 100 ^oC to 180 ^oC for each 10 ^oC. For each geometry, the maximum operating temperature with the safety factor of at least 2 has been reported (Figure 22(a)).

The overall mechanical safety factor of the device can change through two main design approaches: cavity design and implementation of the mechanical supports. We start the design approach by varying the cavity and we conclude that it is challenging to reach temperatures over 150 ^oC without the mechanical support structures. We therefore introduce the mechanical support structures and fine-tune the design to increase the safety factor. The baseline geometry for all simulations is a bare square cavity design with 400 μm cavity thickness, 50 μm fillet radius, 10×10 mm^2 cavity area, and 15×15×1 mm^3 device dimensions.

A) *Effect of Cavity Shape, Cavity Thickness Cavity Area, and Fillet Radius:* To study the effects of the overall design parameters in bare cavity, we explore the effects of decreasing the cavity thickness t_{core}, decreasing the cavity area L_{core}^2, and increasing the fillet radius r_f. Fig. 5 (b) shows the predicted safety factor for t_{core} = 400 μm, L_{core} = 10 mm, and r_f = 10, 50, 100 μm. As shown in the figure, increasing the fillet radius r_f leads to a higher safety factor. This is due to the fact that the higher fillet radius provides more room for the stress distribution in the corners and tolerating the bending moment. The radius of the fillet area is highly dependent on the micro-fabrication process and silicon-etching recipe in particular. Most of the silicon DRIE recipes for etching of the vapor chamber cavity are designed to etch hundreds of microns in a few hours

and will result in sharp cavity edges with fillet radius of close to 50 μm, however; it is possible to use a combination of recipes to achieve high fillet radius in the deep silicon etching. The higher fillet radius does not have a significant effect on the vapor pressure drop or on the thermal performance, however; it can significantly increase the mechanical safety factor of the design and help with tolerating the higher internal pressures. Fig. 25 (c) shows the safety factor as a function of the cavity thickness t_{core} as it has decreased from 600 to 250 μm. The reduction in the cavity thickness does not reduce the bending moment in the corner, however; it helps with increasing the safety factor by providing a better distribution of the stress over a thicker cavity cap. Although increasing the thickness of the cavity wall is not desirable in the ultra-thin vapor chamber application, this parameter can be considered in the design process since even 150 μm addition to the baseline thickness can increase the maximum temperature more than 10 ^{o}C. Fig. 25 (d) shows the calculated safety factor for L_{cavity}^2 = 10×10, 13×13, 14×14 mm^2. Even though increasing the cavity area is highly appealing for the heat spreader and thermal switch application since it provides an extra room for the vapor transport, it will also significantly increase the stress over the corners due to the reduction in the surface areas that tolerate the bending moment. Additionally, the larger cavity area results in a smaller surface area for the bonding between the condenser and evaporator substrates and will increase the need for strong bonding methods to tolerate the tensile stress in the bonding section. Circular cavities have been employed for decades for other applications such as pressure sensors, however; we propose the circular cavity design for the UTVC application here for the first time. Figure 25(e) shows the simulation results of the circular cavity design for circular cavity radius of 10.00 (the circular cavity inscribed in the square cavity), 11.28 (the circular cavity has the same cavity area as the square cavity), and 14.14 mm (the superscribed circular cavity around the square cavity). As shown in the

figure, the circular cavity with the exact same cavity area as the square cavity can increase the maximum working temperature of the device by 5 ^{o}C. This is due to the better stress distribution over the cavity edges in the circular design.

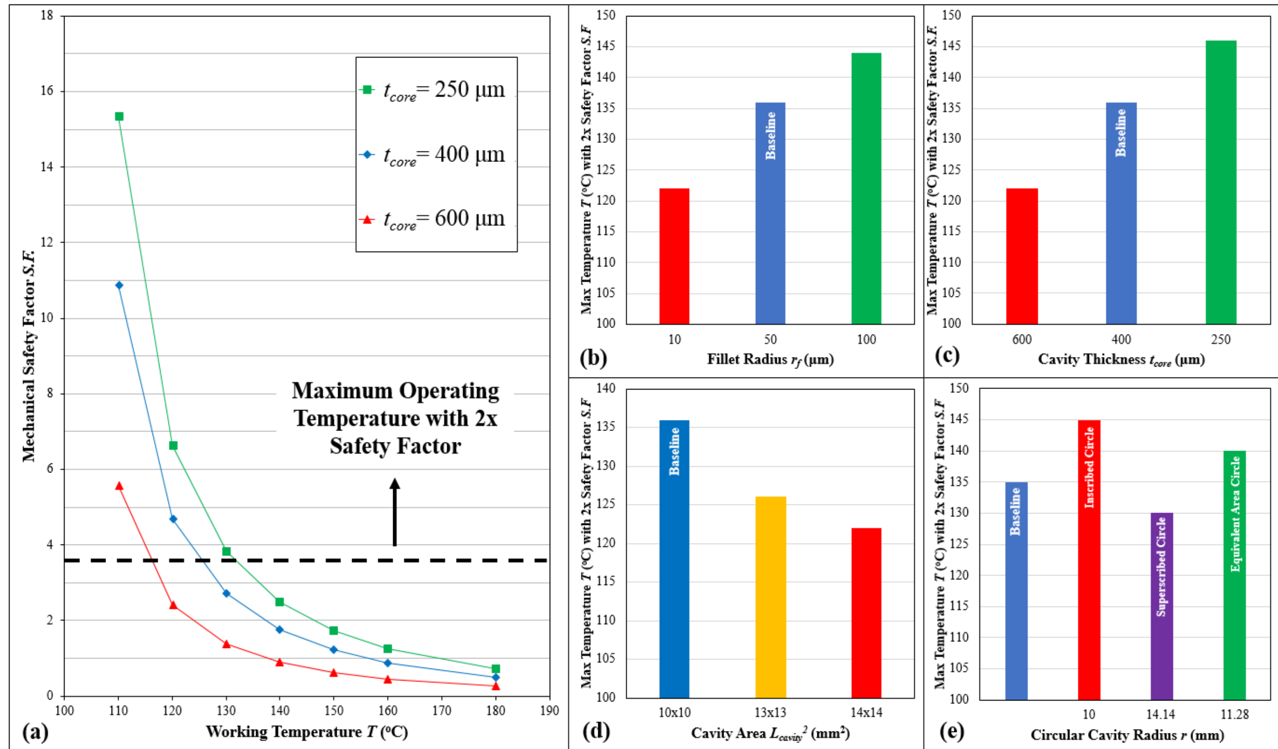

Figure 22. (a) For all of the subsequent mechanical analysis, only one parameter (e.g. cavity thickness t_{core}) is varied per study. A safety factor of at least 2 is reported for the maximum operating temperature for each design. **(b)** Increasing the fillet radius r_f has a significant effect on reducing the maximum stress due to the stress concentration in the cavity edges over in the condenser substrate. **(c)** Decreasing the cavity thickness t_{core} improves the mechanical reliability, however; this will result in a reduction in the thermal performance of the vapor chamber due to the increase in the thickness of the solid silicon wall. **(d)** We prefer a higher cavity/hot spot ratio for better thermal performance, however; a higher cavity area L_{core}^2 increases the bending moment over the cavity edges and results in decreasing the mechanical safety factor. **(e)** The circular cavity design increases the mechanical safety factor by distributing the mechanical load more uniformly. A higher temperature is achievable with the circular design without sacrificing any cavity area (equivalent area circle).

Various cavity geometry and dimensions can help with the reliability of the mechanical design, however; the mentioned design approaches are not effective when a safety factor of more than 2 is required at the temperatures over 150 ^{o}C (Figure 25(b-e)). As we discussed in Figure 21(c), for the baseline geometry, the point with the highest stress appears in the condenser over the cavity edges. This is due to the maximum bending moment in this area and various mechanical support structures can be employed to reduce this moment. Here, we explore the implementation of embedded silicon mechanical support structures inside the device.

B) *Mechanical Support Structure: Ribs, Crossbars, and Micro-Post Arrays:* Rib support structures (Figure 26(a)) seem to be a reasonable choice for the stress reduction in over the cavity edges. However, no significant improvement was observed in the mechanical safety factor (Figure 26(d)). This is because of the fact that the high stress concentration points appear over the root of the ribs (see Appendix). Ribs reduce the effective cavity radius and increase the effective thickness, but an equivalent force should be tolerated in the roots. Therefore, the advantage in the radius reduction is not applicable in the roots, which have a smaller area compared with the original cavity edge. This results in a higher stress concentration. Increasing the area of the roots by using fillets helps with the stress reduction, however; it is equivalent to reducing the cavity area and is not applicable in the parametric study of the ribs.

We therefore considered crossbars as the mechanical support structures. Figure 26(b) shows the crossbars design as the mechanical support. Plus shape configuration of the crossbars (design A) is not effective due to the same reason as the rib supports (i.e. stress concentrates in the roots). However, the cross-shape configuration of the crossbars (design B) is an effective mechanical support since this configuration distributes the stress from the cavity side edges to the corners of the cavity. The combination of the plus and the cross shaped crossbar support is not as

effective as the cross crossbar alone due to, again, the stress concentration in the roots (Figure 26(f)). Figure 26 (c) shows the design of the bonded support structures (i.e. the micro-post arrays). Micro-post structures are etched into the condenser and the evaporator substrates. The support structures need to be bonded across the vapor core area, which requires a high degree of alignment during the bonding process. The micro-post arrays are the most effective mechanical support structures and can increase the working temperature of the device to more than 150 ^{o}C (Figure 26(e)). Figure 26 (g) shows a comparison of the various design approaches. Smaller cavity area L_{core}^2, thinner cavity t_{core}, and higher fillet radius r_f help with increasing the mechanical safety factor. Additionally, a circular cavity provides better stress distribution. A combination of a thin evaporator and a thick condenser can potentially help with the mechanical design. The condenser design can be optimized to increase the safety factor. Micro-post arrays and crossbars can be employed as the mechanical support structures if higher working temperatures are required.

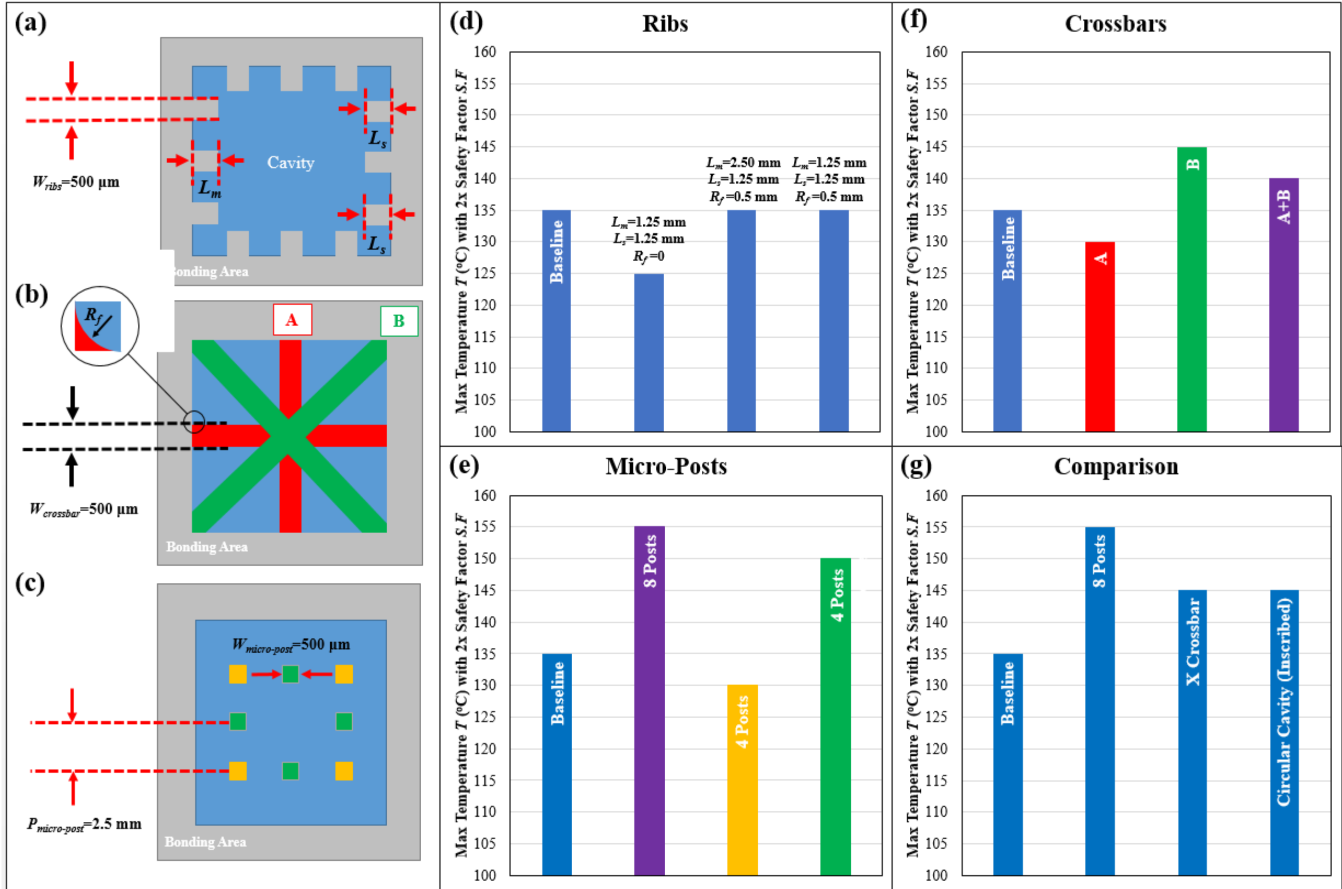

Figure 23. **(a)** Ribs are etched into only the condenser section while the evaporator still has the bare cavity design. The length of the middle rib L_m and the side rib L_s are varied between 1.25-2.50 mm while the width of the ribs W_{ribs} is equivalent to 500 μm for all cases. **(b)** Crossbars are etched into the condenser while the evaporator still has the bare cavity design. Design A consists of the crossbars that are attached to the side of the cavity while the crossbars in design B are attach to the corners of the cavity. **(c)** Micro-post arrays are etched into the condenser and the evaporator and then are bonded together. The micro-posts have a square cross-section with the side dimension $W_{micro\text{-}post}$ of 500 μm. The 8 posts are uniformly distributed inside of the 10×10 mm^2 cavity with the pitch (center to center) distance $P_{micro\text{-}post}$ of 2.5 mm. There is no micro-post in the central region of the cavity to avoid the direct heat conduction from the hotspot to the condenser. **(d)** Different variations of the rib support structure did not have a significant effect on improving the mechanical reliability. This is due to the stress concentration in the root of the ribs. **(e)** Micro-post support structures are highly effective for increasing the mechanical reliability. **(f)** Crossbar design A will result in stress concentration in the roots of the crossbars while design B helps with the distribution of the stress to the corners of the cavity. **(g)** Comparison of the various mechanical

support structures shows that the micro-post configuration is highly effective in increasing the mechanical safety factor. Crossbar and circular cavity design are not as effective as the micro-posts, however; they increase the mechanical reliability without having a negative effect over the thermal performance (e.g. direct heat conduction from evaporator to the condenser, increasing the vapor pressure drop to the sidewalls, etc.)

C) *Critical point of the design, the bonding area:* As we showed in the previous sections, the maximum tensile stress can increase significantly in the silicon vapor chamber by increasing the temperature (e.g. >246 MPa for the baseline cavity at the working temperature of 150 ^{o}C). We presented various design approaches to increase the mechanical reliability of the bare cavity and different mechanical support structures that can help with increasing the safety factor. In all of the presented simulations we assumed a perfect bonding between the evaporator and the condenser. However, in the vapor chamber application, the evaporator and the condenser are usually fabricated separately and then bonded together using various bonding methods and materials [28]. The fracture strength of the bonding area can vary significantly, however; even with the strongest metal bonding methods it is not more than 20 MPa [44-49], while the fracture strength of silicon is at least 300 MPa (see Chapter 1, page 10). Therefore, the bonding section has a significantly lower mechanical strength, is the critical point of the mechanical design, and determines the safety factor of the whole device. In continue, we pay a special attention to the bonding area for the silicon vapor chamber application. We design, fabricate, and conduct the tensile tests for two batch of samples (one for Au-Sn and one for Au-Si bond, each batch consists of 11 samples) that are specifically made for the UTVC application.

4.3. Experimental measurement of bond strength

A. Sample Design

The geometry of the high-performance ultra-thin vapor chamber consists of an evaporator and a condenser. The two substrates are fabricated and then bonded together using wafer-level bonding. We implement a high-density array of the micro-post support structures in the samples to have a more uniform bonding pressure during the bonding process. We use the cross-point configuration of micro-channels in order to mirror the bonding cross-section of micro-post configuration in the vapor chamber while circumventing the alignment challenges in the wafer-level bonding. The sample geometry and the bonding area are shown in Figure 24. The geometry of the bonding area can significantly change the heat transfer and the temperature distribution during the eutectic bonding process. The variation in the bonding temperature will result in a significant difference in the bonding quality and consequently the fracture strength. Therefore, up to 8 different geometries per wafer are designed, where the parameters are outlined in Table 2. Sidewall thickness is 350 μm and the bonding area is 10-28% of the sample base surface area.

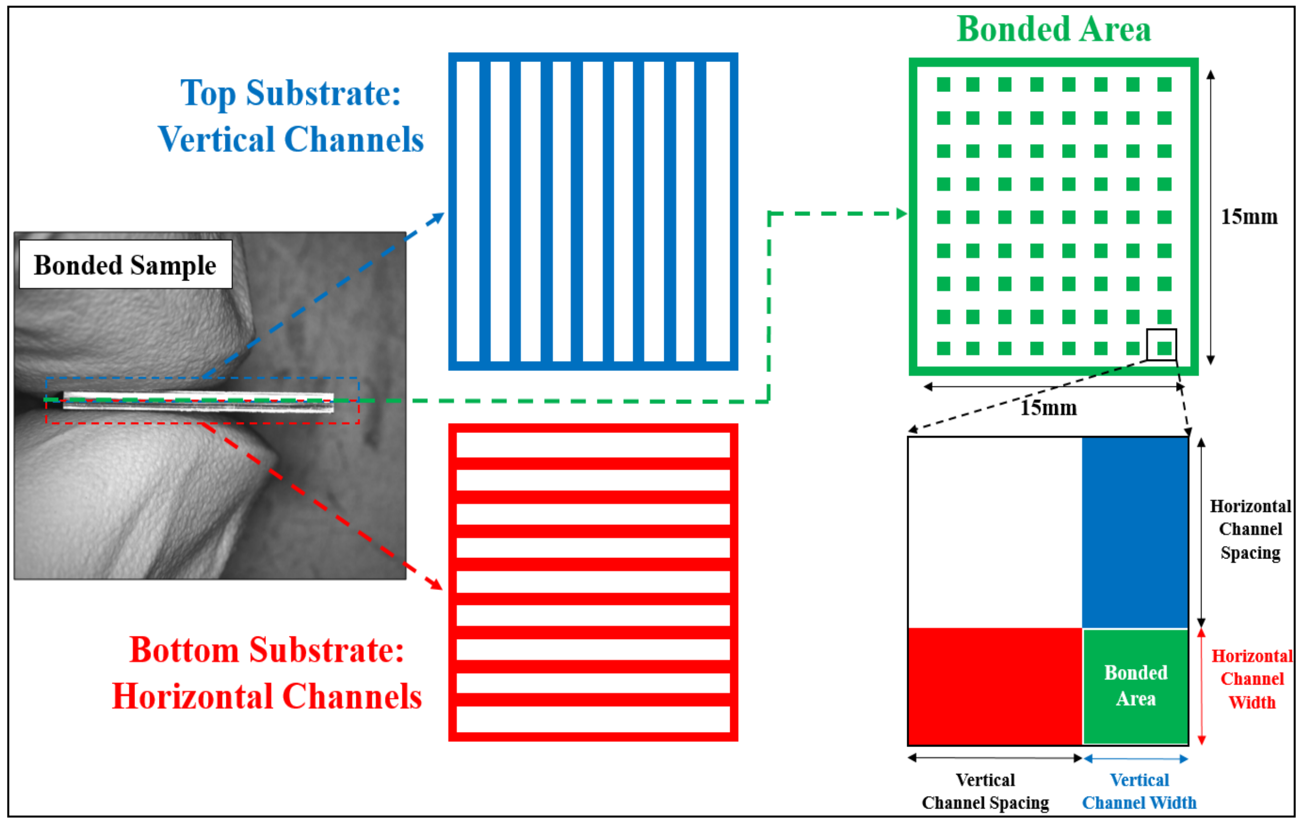

Figure 24. Sample design and the bonding interface: (**Left**) Full sample with a total surface area of 15×15 mm^2 and total thickness of 1 mm. (**Middle**) Vertical and horizontal micro-channels are fabricated over separate substrates and then bonded together. **(Right)** Bonded area between the substrates representing the bonding interface of the micro-post arrays in the ultra-thin vapor chamber application. This design helps with controlling the bonding cross section by changing the vertical and horizontal channel width and spacing.

B. Sample Fabrication

The sample fabrication process starts with a general cleaning process of the 4-inch prime silicon wafers with 500 μm total thickness. Wafers are put in a piranha solution consists of 90% H_2SO_4 and 10% H_2O_2 at the temperature of 120 ^oC for at least 20 minutes. Then, the wafers are spray rinsed with water for at least 10 minutes and put into a spin-rinse-drier machine (SRD) for an extra 10 minutes. This cleaning process helps with the removal of any dust and organic contaminants. In continue, Hexamethyldisilizane (HMDS) is deposited over the wafers in a vacuum oven at the temperature of 150 ^oC to increase the hydrophobicity of the surface and help with better coating and adhesion of the polymer photoresist (PR) in the next step. In continue, 1.6 μm of SPR3612 PR is coated over the silicon wafers using spin coating for 90 seconds. A Heidelberg MA150 is used for the patterning of the micro-channels with 500 nm resolution and maskless exposure. Afterward, the substrates are etched up to 15 μm based on the Bosch process and using a DRIE etching machine. Since in this study we are focusing on the fracture strength measurement of the samples, the etching depth does not have any significant effect on our measurements. Using a wet furnace (O_2 and H_2O at the ambient pressure) at the temperature of 900 ^oC, a layer of SiO_2 was grown up to 1000 Å thickness for approximately 2 hours. The oxide growth has been conducted for both the top and the bottom wafers in Au-Sn bonding to make a diffusion barrier for silicon in the Au-Sn eutectic reaction. On the other hand, diffusion of silicon is appealing in the Au-Si bonding, however; we still grow the oxide layer over one of the wafers in order to limit the ratio of the silicon in the Au-Si eutectic reaction (figure 25 (a)). In the next step, for Au-Sn bonding, using a thin film metal evaporator, we deposit Ti, Au, Sn, and Au, with the thickness of 200 Å, 1500 Å, 750 Å, and 1500 Å, respectively. The layers are deposited on both the top and the bottom wafers using the electron-beam evaporator. In the Au-Sn bonding, the layers are deposited in a sandwich composition for increasing the contact area between gold and tin, a better mixture of the bonding materials at the eutectic temperature and providing a more uniform bonding. For the Au-Si bonding, 200 Å of Ti and 5000 Å of Au are deposited on both of the wafers (Figure 25 (b)). The role of the titanium layer in

both of the bonding methods is to increase the adhesion of the gold layer to the silicon wafer. Due to the low thickness of the bonding material, surface cleanness is crucial during the fabrication process and the bonding. We, therefore, implement multiple cleaning processes before the start of the fabrication, after the etching process, before and after the oxide growth, and before the metal deposition. The cleaning process before the eutectic bonding includes submersion of the wafers in SRS-1000 at the temperature of 40 ^{o}C for 20 minutes (for removal of the organic contaminants), followed by SRD for 10 minutes. Additionally, the wafers are cleaned with a mega sonic cleaner before the bonding for 3 minutes for removal of any micro-scale particles. Afterward, the substrates are aligned with a precision of fewer than 20 μm. The eutectic bonding process starts with pumping down the chamber to 10^{-3} Torr followed by Nitrogen purging for the removal of the leftover air. The two substrates are then heated up to the temperature of 350 ^{o}C at a pressure of less than 10^{-4} Torr. The low pressure prevents the possible oxidation of the tin layer or additional oxide growth over the silicon during the bonding process. The eutectic bonding process has been performed using a uniform uniaxial compressive force of 3340 N (equivalent uniform pressure of 0.4 MPa over the 4-inch wafer) for 20 minutes. Then, the load is removed, and the cooling of the chamber has been done based on the natural convection. Wafers are taken out of the chamber at a temperature of less than 30 ^{o}C after 4 hours of cooling. To prevent the effect of variation in the fabrication process, all of the samples for each bonding method are fabricated and bonded over the same wafer. The fabrication of the samples has been performed in a class 2 cleanroom (<100 ppm dust density).

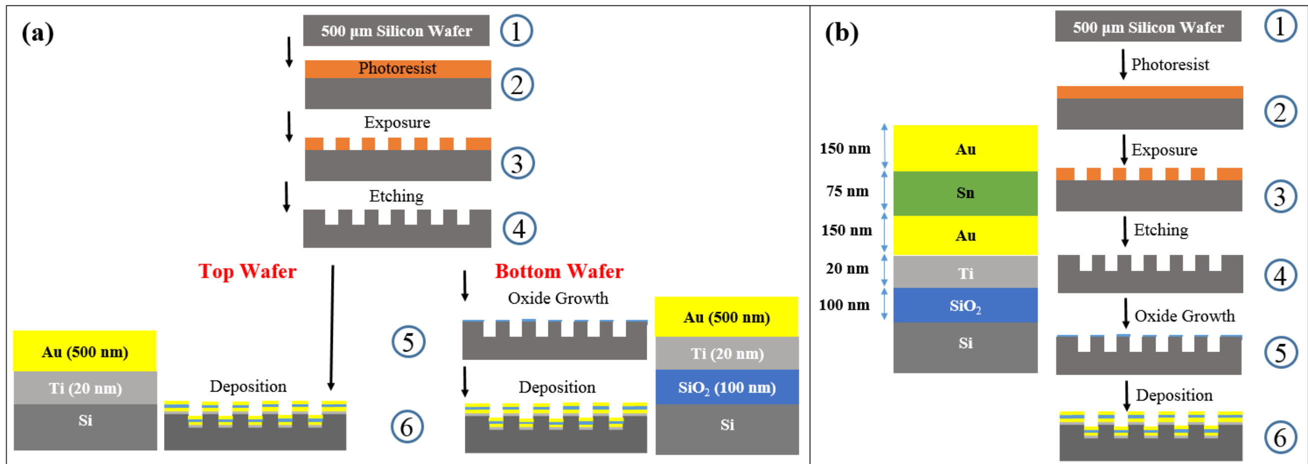

Figure 25. The fabrication process for **(a)** Au-Si and **(b)** Au-Sn bonding includes (steps 1, 2) the spin coating of photoresist, (step 3) exposure with a Heidelberg MA150, (step 4) RIE etching up to 15 μm, and thermal oxide growth for 100 nm. The fabrication process for Au-Si bonding is very similar to Au-Sn bonding except in the oxide growth (step 5), only one of the wafers is oxidized to provide silicon in the eutectic reaction from the other wafer. The composition of the bonding layer for Au-Sn bonding is the same for both the top and the bottom wafer, however; for the Au-Si bonding, the oxide layer does not exist over one of the wafers (step 6).

C. Tensile Test Setup

The bonding area between the evaporator and the condenser undergoes a tensile stress in the vapor chamber application. To apply a uniform, normal, tensile stress over the surface area of the bonding section, we designed and fabricated a setup using aluminum, silicone rubber (McMaster-Carr, Product No. DSP4038GP), and steel-reinforced epoxy (JB Weld^{TM}, Cold Weld^{TM} Product No. 8280) (Figure 26(a)). The set of aluminum holders are designed to attach the sample holder configuration to the grippers of the Instron tensile tester. A set of steel plates is screwed to the aluminum to eliminate the need for changing the whole gripper structure for each sample and help with the preparation and testing of multiple samples with the same setup. In our recent study [46], we implemented a 4-layer configuration of steel-reinforced epoxy and silicone gaskets to attach the samples to the metal plates. In this study, however; an extra layer of a metal plate on each side is implemented to distribute the stress and use the shear strength of the epoxy (Figure 26(b)). The tensile testing has been conducted and tensile force, displacement and time are directly measured with force measurement accuracy of 0.4% and strain measurement accuracy of 0.5%. Multiple considerations in the design and fabrication of the tensile test setup such as the fracture strength characterization for the epoxy, epoxy-sample bond, epoxy-steel plate bond, and the sample angle with the horizon are provided in the Appendix (Figure A1-A4).

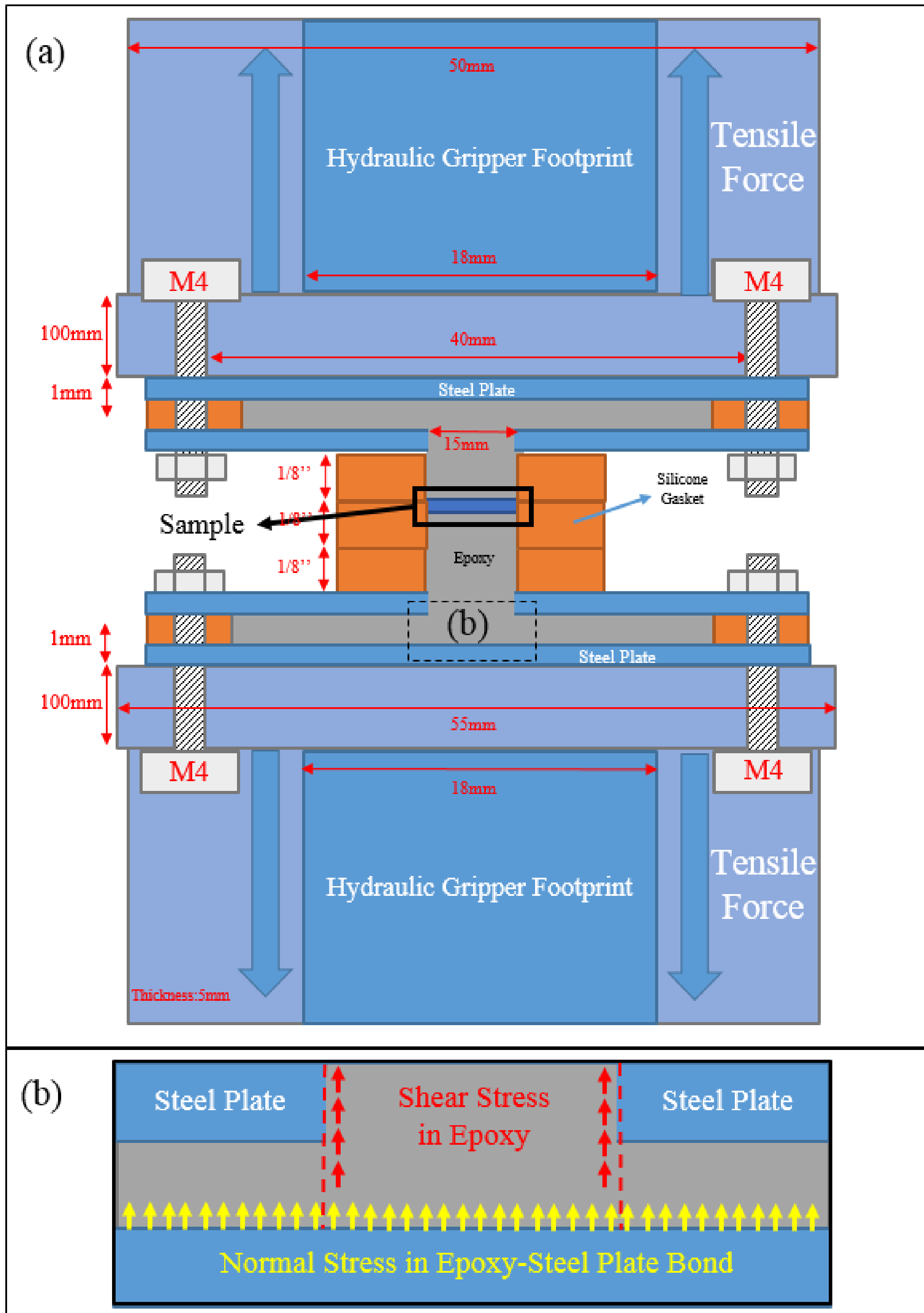

Figure 26. (a) Design of the tensile test setup: hydraulic grippers of Instron tester apply the tensile force over the silicone-epoxy-sample configuration using the aluminum holders. The configuration allows the fracture strength measurement of the bonding area for samples with small thickness and large surface area.

(b) Epoxy to steel plate bonding: due to the low fracture strength of the epoxy-steel plate bond (~3 MPa, see Appendix), the configuration in our previous study [46] breaks at the epoxy-steel plate section (instead of the evaporator-condenser bonding area) when fracture strength measurements of >12 MPa are required. Therefore, in the present study, we implemented another layer of steel plate to increase surface area and rely on the additional shear strength of the steel-reinforced epoxy instead of solely relying on the epoxy-steel plate bond strength.

I. FRACTURE STRENGTH CHARACTERIZATION

Tensile tests were conducted for 22 samples and the average fracture strength for the Au-Sn and Au-Si bonding were 13.2 and 20.2 MPa, respectively (see Table 4). The cross-section of the bonding area after the tensile test showed the high precision of the alignment during the bonding and the accurate placement of the samples inside the tensile test setup (see Figure A4 in Appendix). Substrates with smaller bonding areas (i.e. lower number of channels or smaller channel width) can be fabricated to achieve higher fracture strength measurements with the current setup. Moreover, various bonding temperatures can be explored in future studies. As shown in Figure 27, the fracture strength of the bonding area reported in the current study is higher the previous studies in the literature [45-49] and paves the way for the design and fabrication of the vapor chambers for high temperature working conditions.

Table 4. Sample geometry, bonding area, and average fracture strength of the samples for Au-Sn (S1-S11) and Au-Si (T1-T11) bonding

Sample ID	Horizontal Channel Width (μm)	Horizontal Channel Spacing (μm)	Vertical Channel Width (μm)	Vertical Channel Spacing (μm)	Bonding Surface Area (mm^2)	Au-Sn (S1-S11)		Au-Si (T1-T11)	
						Ultimate Tensile Force (N)	Ultimate Tensile Stress (MPa)	Ultimate Tensile Force (N)	Ultimate Tensile Stress (MPa)
S1/T1	100	100	150	150	66.9	658.4	9.8	822.5	12.3
S2/T2	100	200	150	150	48.1	796.3	16.5	1159.8	24.1
S3/T3	150	150	150	150	66.9	1031.8	15.4	1925.9	28.8
S4/T4	150	150	100	150	55.6	889.4	16.0	1023.5	18.4
S5/T5	100	100	100	150	55.6	547.9	9.9	901.1	16.2
S6/T6	100	200	100	150	40.6	716.2	17.6	824.6	20.3
S7/T7	150	150	100	150	55.6	1014.8	18.2	1479.6	26.6
S8/T8	100	100	100	150	55.6	556.2	10.0	839.9	15.1
S9/T9	100	100	50	200	33.1	221.7	6.7	526.6	15.9
S10/T10	100	200	50	200	25.6	173.7	6.8	351.0	13.7
S11/T11	150	150	50	200	33.1	589.6	17.8	1016.9	30.7
Average fracture strength of the samples						654.2	13.2	988.3	20.2
Standard Error						81.1	1.3	123.8	1.8

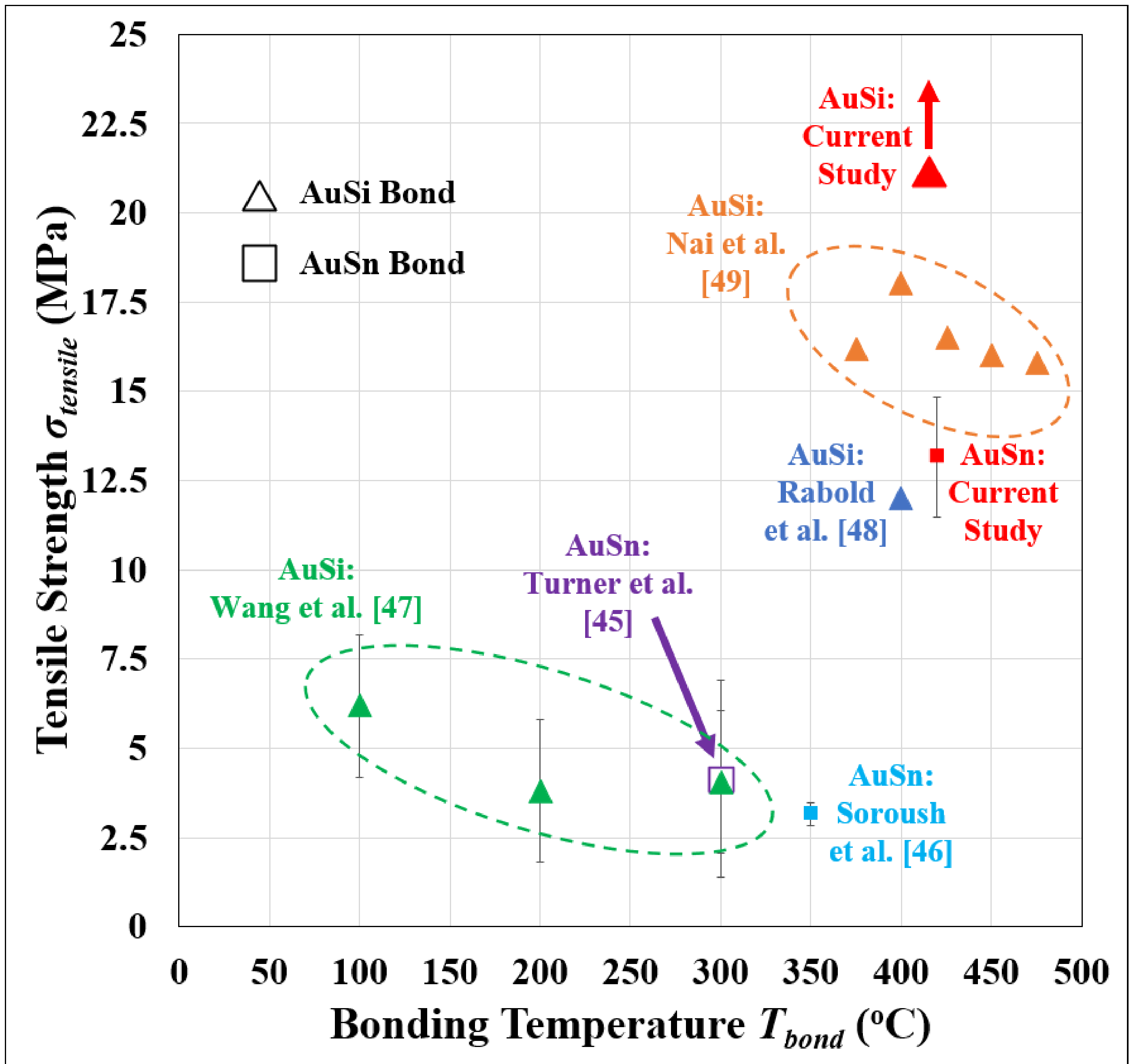

Fig. 27. Tensile test results for Au-Sn and Au-Si bonding: The average fracture strength for Gold-Tin eutectic bonding at 420 °C is 13.2 MPa (higher than the previous studies [45, 46]). The measured fracture strength for gold-silicon eutectic bonding at 420 °C is over 20.2 MPa (higher than the previous studies [47-49]). As shown, the bonding temperature has a significant effect on the bonding strength.

Chapter 5

Conclusion and Future Work

5.1. Contact angle engineering

While a hybrid micro porous structure of copper inverse opals (CIOs) and copper wire meshes (CWMs) is a promising choice as a high-performance evaporator wick, maintaining the hydrophilicity of the wick presents a challenge in capillary-fed boiling application. In this study, we investigated the contact angle change of untreated copper and copper oxides under various conditions. To avoid the formation of hydrophobic Cu_2O, we pre-oxidized the copper micro porous structure to form hydrophilic cupric oxide CuO. We studied the effect of various thermal and chemical oxidation recipes on the morphology of the resulting structures. A chemical oxidation formula was implemented and fine-tuned for the creation of a highly stable superhydrophilic surface for copper inverse opals (CIOs) and copper wire meshes. The CuO nano needles created using the final recipe have a length of <100 nm and do not cause closure of the necks (~1 μm diameter). The hybrid structure of copper inverse opals and copper wire meshes can be used in various field applications such as the evaporator component in ultra-thin vapor chambers for heat spreading or thermal switch devices. In the areas where the lifetime of years is expected, mechanical reliability of the oxide layer and retaining hydrophilicity are the critical issues that need to be addressed. As future work, long term reliability of the oxide layer, and composition analysis of the nano-needles structure can be studied.

5.2. Hybrid Porous Wicks

While the CHF for the single layer wire mesh is less than 30 Wcm^{-2}, a hybrid structure of CWMs and CIOs can provide over 20 times increase in the CHF and 15 times reduction in the thermal resistance. The fabrication process for CWMs-CIOs hybrid evaporator wick is low cost, low temperature (<70 ^{o}C), and scalable, showing promise for mass manufacturing and industrial applications. For the future studies, process development for higher quality CIOs, multiphysics coupled modeling, optimizing pore

ratios for the bio-porous wick, and develop of multi-level multi-pore wicks with variant thickness can be investigated.

5.3. Reliable vapor chamber

We conducted a parametric study for thermo-mechanical design of silicon ultra-thin vapor chambers. The model showed an increase in the mechanical safety factor by reducing the cavity thickness, cavity area and increasing the fillet radius. To further increase reliability, we investigated implementation of mechanical support structures such as ribs, crossbars and micro-posts. Rib support structures were not effective, however; micro-posts were highly appealing for the stress reduction. In order to investigate the reliability of the bonding area, a tensile test setup was designed and fabricated. The samples specifically were designed for the ultra-thin vapor chamber application. Gold-tin and gold-silicon eutectic bonding were used as the bonding interface material. For future studies, thermal gradients can be implemented in the model and the effect of the support structures on the thermal performance, warpage, and pressure drop can be studied. Even higher strength can be reached by exploring various temperatures or layer compositions (e.g. increasing the tin ratio significantly increases the strength of gold-tin eutectic bond). Silicon-silicon direct bonding is another type of bonding that is worth investing for silicon-based vapor chambers.

Bibliography

[1] Cho, Sangbeom, and Yogendra Joshi. "Thermal Performance of Microelectronic Substrates With Submillimeter Integrated Vapor Chamber." Journal of Heat Transfer 141.5 (2019).

[2] Jung, Yoon Seok, et al. "Improved functionality of lithium-ion batteries enabled by atomic layer deposition on the porous microstructure of polymer separators and coating electrodes." Advanced Energy Materials 2.8 (2012): 1022-1027.

[3] Pham, Q. N., et al. "Microscale liquid transport in polycrystalline inverse opals across grain boundaries." Scientific reports 7.1 (2017): 1-9.

[4] Chang, Feng-Ming, et al. "Superhydrophilicity to superhydrophobicity transition of CuO nanowire films." Applied Physics Letters 96.11 (2010): 114101.

[5] Zhou, Feng, et al. "Vapor chamber with thermal diode and switch functions." 2017 16th IEEE Intersociety Conference on Thermal and Thermomechanical Phenomena in Electronic Systems (ITherm). IEEE, 2017.

[6] Nam, Youngsuk, and Y. Sungtaek Ju. "A comparative study of the morphology and wetting characteristics of micro/nanostructured Cu surfaces for phase change heat transfer applications." Journal of Adhesion Science and Technology 27.20 (2013): 2163-2176.

[7] Huang, Ding-Jun, and Tzong-Shyng Leu. "Fabrication of high wettability gradient on copper substrate." Applied Surface Science 280 (2013): 25-32.

[8] Long, Jiangyou, et al. "Wettability conversion of ultrafast laser structured copper surface." Journal of Laser Applications 27.S2 (2015): S29107.

[9] Dubey, Pranav P., et al. "Controlled wetting properties through heterogeneous surfaces containing two-level nanofeatures." ACS omega 2.11 (2017): 7916-7922.

[10] Pham, Quang N., et al. "Hierarchical and well-ordered porous copper for liquid transport properties control." ACS applied materials & interfaces 10.18 (2018): 16015-16023.

[11] Nam, Youngsuk, and Y. Sungtaek Ju. "A comparative study of the morphology and wetting characteristics of micro/nanostructured Cu surfaces for phase change heat transfer applications." Journal of Adhesion Science and Technology 27.20 (2013): 2163-2176.

[12]http://www.1-act.com/advancedtechnologie-s/heat-pipes/vapor-chambers.php- Advanced Cooling Technologies, Inc.

[13] http://www.celsiatechnologies.com/nanospreader_technology.asp -- Celsia

[14] Weibel, Justin A., Suresh V. Garimella, and Mark T. North. "Characterization of evaporation and boiling from sintered powder wicks fed by capillary action." International Journal of Heat and Mass Transfer 53.19-20 (2010): 4204-4215.

[15] Bar-Cohen, A., Matin, K., Bloschock, K., Jankowski, N., Sharar, D., 2013, "Two-Phase Thermal Ground Planes: Technology Development and Parametric Results," Final Report DOC# 21479: DARPA, Thermal Ground Plane (TGP).

[16] Sudhakar, S., Weibel, J.A., Zhou, F., Dede, E.M. and Garimella, S.V., 2019. Area-scalable high-heat-flux dissipation at low thermal resistance using a capillary-fed two-layer evaporator wick. International Journal of Heat and Mass Transfer, 135, pp.1346-1356.

[17] Wen, Rongfu, et al. "Capillary-driven liquid film boiling heat transfer on hybrid mesh wicking structures." Nano Energy 51 (2018): 373-382.

[18] Palko, J.W., Zhang, C., Wilbur, J., Dusseault, T.J., Asheghi, M., Goodson, K.E., and Santiago, J.G., 2015, "Approaching the Limits of Two-Phase Boiling Heat Transfer: High Heat Flux and Low Superheat," Appl. Phys. Lett., 107, 253903.

[19] Zhang, C., Palko, J.W., Rong, G., Pringle, K.S., Barako, M.T., Dusseault, T.J., Asheghi, M., Santiago, J.G. and Goodson, K.E., 2018. "Tailoring permeability of microporous copper structures through template sintering". ACS applied materials & interfaces.

[20] Zhang, C., Palko, J.W., Barako, M.T., Asheghi, M., Santiago, J.G. and Goodson, K.E., 2018. "Enhanced Capillary-Fed Boiling in Copper Inverse Opals via Template Sintering". Advanced Functional Materials.

[21] Wu, Q., Zhang, C., Asheghi, M., Goodson, K.E., 2020. "Design and fabrication of graded copper inverse opals (G-CIOs) for capillary-fed boiling in high heat flux cooling applications." International Technical Conference and Exhibition on Packaging and Integration of Electronic and Photonic Microsystems. American Society of Mechanical Engineers Digital Collection.

[22] Zhang, Chi, et al. "Design and optimization of well-ordered microporous copper structure for high heat flux cooling applications." International Journal of Heat and Mass Transfer 173 (2021): 121241.

[23] Espinosa, F. A. D.; Peters, T. B.; Brisson, J. G. Effect of Fabrication Parameters on the Thermophysical Properties of Sintered Wicks for Heat Pipe Applications. Int. J. Heat Mass Transfer 2012, 55, 7471−7486."

[24] Weibel, J. A., et al. "Carbon nanotube coatings for enhanced capillary-fed boiling from porous microstructures." Nanoscale and Microscale Thermophysical Engineering 16.1 (2012): 1-17.

[25] Sudhakar, S., Weibel, J.A. and Garimella, S.V., 2019. Experimental investigation of boiling regimes in a capillary-fed two-layer evaporator wick. International Journal of Heat and Mass Transfer, 135, pp.1335-1345.

[26] Li, C. and Peterson, G.P., 2006. Evaporation/boiling in thin capillary wicks (II)—effects of volumetric porosity and mesh size.

[27] Lv, L. and Li, J., 2017. Managing high heat flux up to 500 W/cm2 through an ultra-thin flat heat pipe with superhydrophilic wick. Applied Thermal Engineering, 122, pp.593-600.

[28] Liu, Tanya, Mehdi Asheghi, and Kenneth E. Goodson. "Performance and Manufacturing of Silicon-Based Vapor Chambers." Applied Mechanics Reviews 73, no. 1 (2021): 010802.

[29] Liu, Tanya, James W. Palko, Joseph S. Katz, Feng Zhou, Ercan M. Dede, Mehdi Asheghi, and Kenneth E. Goodson. "Steady-State Parametric Optimization and Transient Characterization of Heat Flow Regulation With Binary Diffusion." IEEE Transactions on Components, Packaging and Manufacturing Technology 10, no. 12 (2020): 1996-2007.

[30] Liu, Tanya, Marc T. Dunham, Ki Wook Jung, Baoxing Chen, Mehdi Asheghi, and Kenneth E. Goodson. "Characterization and thermal modeling of a miniature silicon vapor chamber for die-level heat redistribution." International Journal of Heat and Mass Transfer 152 (2020): 119569.

[31] Cai, Qingjun, Bing-chung Chen, and Chialun Tsai. "Design, development and tests of high-performance silicon vapor chamber." Journal of Micromechanics and Microengineering 22, no. 3 (2012): 035009.

[32] Cai, Steve Q., Ya-Chi Chen, and Avijit Bhunia. "Design, development and tests of a compact thermofluid system." Applied Thermal Engineering 102 (2016): 1320-1327.

[33] Wei, Mengyao, Bin He, Qian Liang, Sivanand Somasundaram, Chuan Seng Tan, and Evelyn N. Wang. "Study of Ultra-thin silicon micropillar based vapor chamber." Proc. World Congr. Mech. Chem. Mater. Eng. (2017): 1-8.

[34] Moser, Benedikt, K. Wasmer, L. Barbieri, and J. Michler. "Strength and fracture of Si micropillars: A new scanning electron microscopy-based micro-compression test." Journal of materials research 22, no. 4 (2007): 1004-1011.

[35] DelRio, Frank W., Robert F. Cook, and Brad L. Boyce. "Fracture strength of micro- and nano-scale silicon components." Applied Physics Reviews 2, no. 2 (2015): 021303.

[36] Chong, Desmond YR, W. E. Lee, B. K. Lim, John HL Pang, and T. H. Low. "Mechanical characterization in failure strength of silicon dice." In The Ninth Intersociety Conference on Thermal and Thermomechanical Phenomena In Electronic Systems (IEEE Cat. No. 04CH37543), vol. 2, pp. 203-210. IEEE, 2004.

[37] Wu, J. D., C. Y. Huang, and C. C. Liao. "Fracture strength characterization and failure analysis of silicon dies." Microelectronics Reliability 43, no. 2 (2003): 269-277.

[38] McLaughlin, J. C., and A. F. W. Willoughby. "Fracture of silicon wafers." Journal of Crystal Growth 85, no. 1-2 (1987): 83-90.

[39] Hopcroft, Matthew A., William D. Nix, and Thomas W. Kenny. "What is the Young's Modulus of Silicon?." Journal of microelectromechanical systems 19, no. 2 (2010): 229-238.

[44] Kim, Jongpal, Dong-il Dan Cho, and Richard S. Muller. "Why is (111) silicon a better mechanical material for MEMS?." In Transducers' 01 Eurosensors XV, pp. 662-665. Springer, Berlin, Heidelberg, 2001.

[45] Turner, Kevin T., Richard Mlcak, David C. Roberts, and S. Mark Spearing. "Bonding of bulk piezoelectric material to silicon using a gold-tin eutectic bond." MRS Online Proceedings Library Archive 687 (2001).

[46] Soroush, Farid, Ki Wook Jung, Madhusudan Iyengar, Chris Malone, Mehdi Asheghi, and Kenneth Goodson. "Mechanical Design and Reliability of Gold-Tin Eutectic Bonding for Silicon-Based Thermal Management Devices." In 2020 19th IEEE Intersociety Conference on Thermal and Thermomechanical Phenomena in Electronic Systems (ITherm), pp. 957-962. IEEE, 2020.

[47] Wang, Ying-Hui, Jian Lu, and Tadatomo Suga. "Low-temperature wafer bonding using gold layers." In 2009 International Conference on Electronic Packaging Technology & High Density Packaging, pp. 516-519. IEEE, 2009.

[48] Rabold, Martin, Holger Kuster, Peter Woias, and Frank Goldschmidtboeing. "Low Temperature Wafer Bonding: Plasma Assisted Silicon Direct Bonding vs. Silicon-Gold Eutectic Bonding." ECS Transactions 16, no. 8 (2008): 499.

[49] Nai, S. M. L., J. Wei, P. C. Lim, and C. K. Wong. "Silicon-to-silicon wafer bonding with gold as intermediate layer." In Proceedings of the 5th Electronics Packaging Technology Conference (EPTC 2003), pp. 119-124. IEEE, 2003.

[50] Tanaka, Katsuhiko, Takahiro Konishi, Masato Ide, and Susumu Sugiyama. "Wafer bonding of lead zirconate titanate to Si using an intermediate gold layer for microdevice application." Journal of Micromechanics and Microengineering 16, no. 4 (2006): 815.

[51] Takagi, H., Kikuchi, K., Maeda, R., Chung, T. R., & Suga, T. (1996). “Surface activated bonding of silicon wafers at room temperature.” Applied physics letters, 68(16), 2222-2224.

[52] https://mcubemems.com/technology/monolithic-mems/

[53] Song, Jing-She, and Mitchell A. Winnik. "Cross-linked, monodisperse, micron-sized polystyrene particles by two-stage dispersion polymerization." Macromolecules 38.20 (2005): 8300-8307

Appendix I: Heater/RTD fabrication and calibration

Fabrication process for serpentine heater and RTD ((Resistance Temperature Detector) sensors are shown in Figure 1. Calibration process for the sensors before conducting the thermal tests is shown in Figure 2.

We used Stanford Nanofabrication Facilities (SNF) and Stanford Nano Shared Facilities (SNSF) for much of the fabrication process. We used Thermco3 for oxide growth, HMDS Vapor Prime Oven (YES) for polymer coating, SVG Resist Coat for automatic photoresist coating, Headway 3 Manual Resist Spinner for manual spin coating, White Oven for manual photoresist development, Heidelberg MLA 150 for exposure, AJA, KJA and Innotec for metal evaporation, Wet Bench for photoresist removal, EV Group Contact Aligner for alignment, EV Group Wafer Bonder for bonding, and DISCO Wafer Saw for dicing.

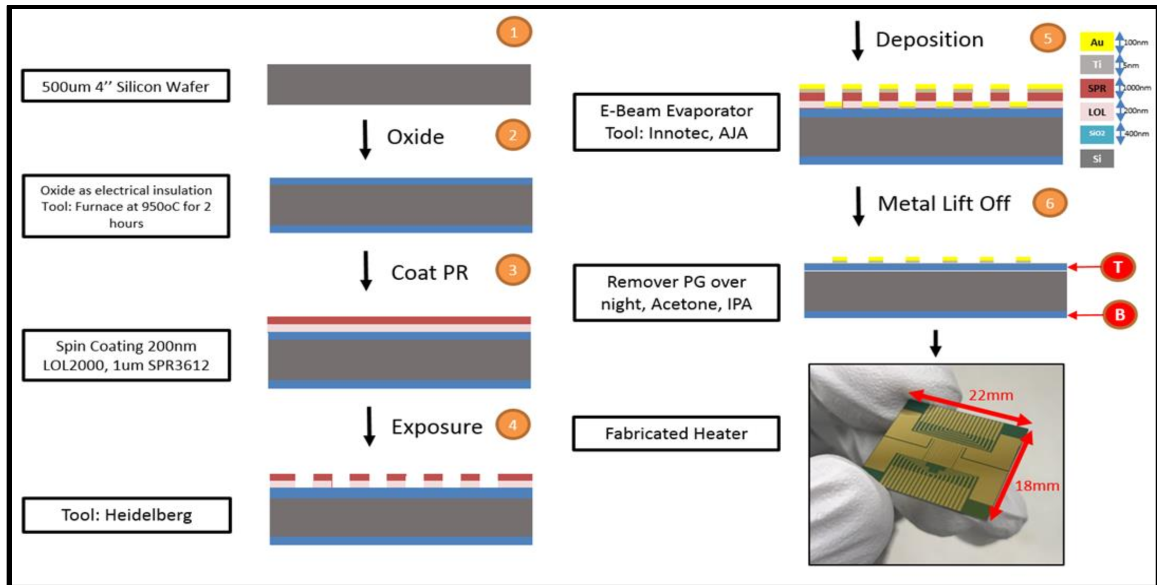

Figure 1. Fabrication process for heater and RTDs: 1. We start with 4'' silicon wafers with 500 µm thickness 2. Natural oxide is grown over the wafers for 450 nm in furnace at 950°C for two hours (oxidation in H_2O and O_2) 3. A layer LOL2000 with 200 nm thickness and then a layer of SPR3612 with 1um thickness is coated over the wafer 4. Pattern is exposed using a maskless UV laser exposure tool 5. 5 nm of Ti and 100 nm of Au are deposited over the wafer using E-Beam evaporator 6. Wafer is left in Remover PG over 12 hours, then sonicated in acetone bath for 5 minutes, then rinsed with IPA and water. At the end, wafers are dried in SRD (spin rinse drier) for 10 minutes.

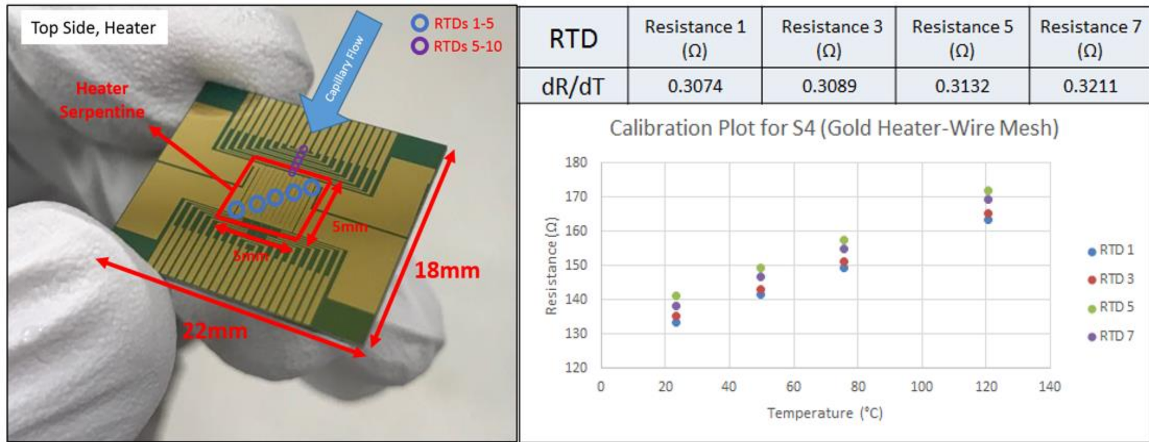

RTD	Resistance 1 (Ω)	Resistance 3 (Ω)	Resistance 5 (Ω)	Resistance 7 (Ω)
dR/dT	0.3074	0.3089	0.3132	0.3211

Figure 2. Calibration Process: Calibration of the RTDs has been done in a temperature-controlled heating bath based on 4-wire measurement from 20 °C to 120 °C with 0.1 °C precision. A sample set of results for a calibration process is shown in the plot. Slope of the resistance-temperature curve is constant and correlation is linear.

Appendix II: Considerations in tensile tests and modeling

Several considerations in design and fabrication of the tensile test setup are presented here. Fracture strength characterization for the epoxy, epoxy-sample bond, and epoxy-steel plate bond are shown in Fig. A1, A2, and A3, respectively. Sample bonding area after the tensile test and the sample angle with the horizon are shown in figure A4. Figure A5 shows a sample simulation result for the rib configuration and explains the reason behind the ineffectiveness of this type of support structure for the vapor chamber application.

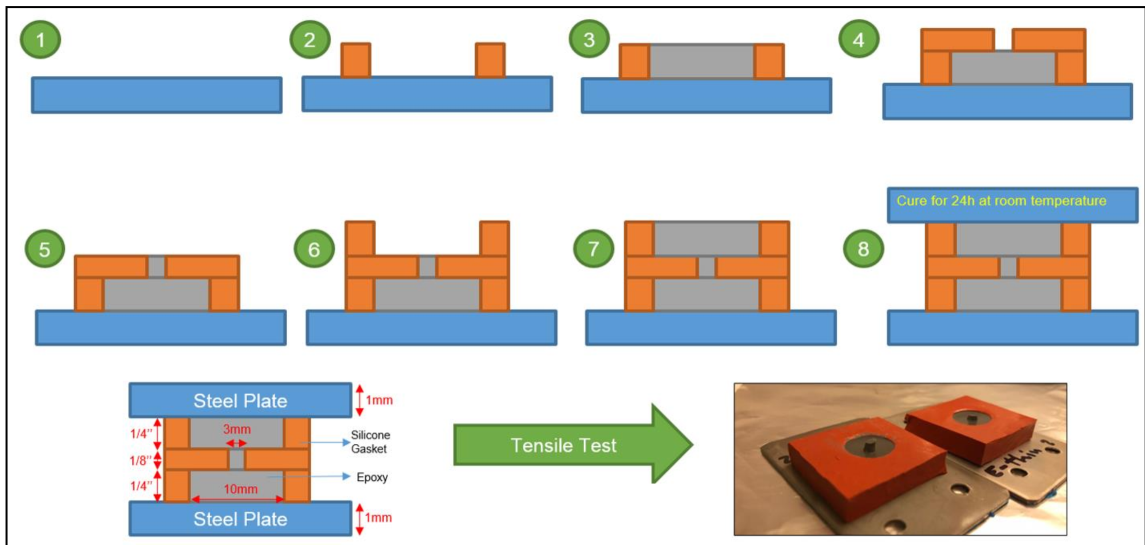

Figure A1. Sample preparation steps for the epoxy characterization: (1) First steel plate (2) First silicone well with 10 mm diameter hole (3) Pouring epoxy and swiping a laser blade over the top for flatness (4) Second silicone well with 3 mm diameter hole (5) Pouring epoxy and swiping a blade for flatness (6) Third silicone well with 3 mm diameter hole (7) Pouring epoxy and swiping a blade for flatness (8) Second steel plate and curing for 24 hours at the room temperature. At the end, the tensile test is conducted and the measured fracture strength for the epoxy is 35 MPa which is very close to the reported value by the commercial vender (34.7 MPa, JB Weld^{TM}, Cold Weld^{TM} Product No. 8280)**.**

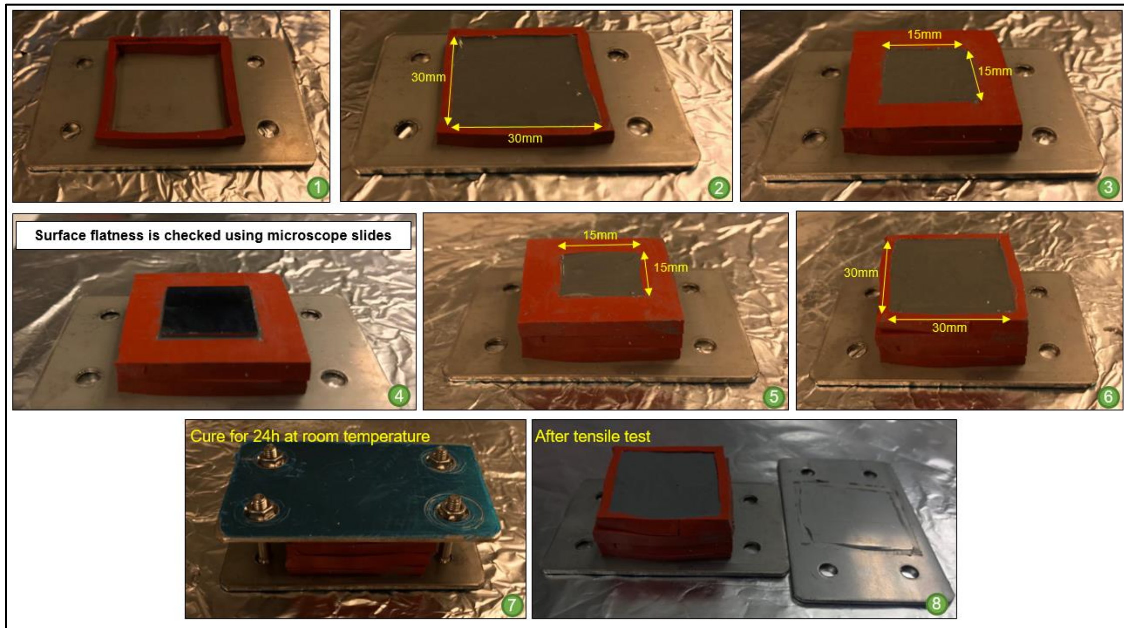

Figure A2. Sample preparation steps for the fracture strength characterization of the bonding between epoxy and sample: (1) The first silicone layer is pressed over the steel plate. (2) The 30×30 mm^2 cavity is filled with epoxy and a blade is swept over the silicone in order to ensure the surface flatness. (3) Another layer of silicon gasket with 15×15 mm^2 cavity area is pressed over the previous layer and a blade is swept over the silicone in order to ensure the surface flatness. (4) The sample is placed over the epoxy layer and the surface flatness is double checked with microscope slides. (5) Another layer of silicone gasket with 30×30 mm^2 cavity area is placed over the previous layer and filled with epoxy. (6) Another layer of silicone gasket with 15×15 mm^2 cavity area is placed over the previous layer and filled with epoxy. (7) The second steel plate is placed over the silicone gasket and tightened with skews. The epoxy is cured at the room temperature for 24 hours. (8) In the tensile testing, the sample broke in the epoxy-steel plate bonding area. The stress the epoxy-steel plate bonding area was ¼ of stress in epoxy-sample section, therefore, the fracture strength of the epoxy-sample bond is at least 4 times higher than the epoxy-steel plate bond.

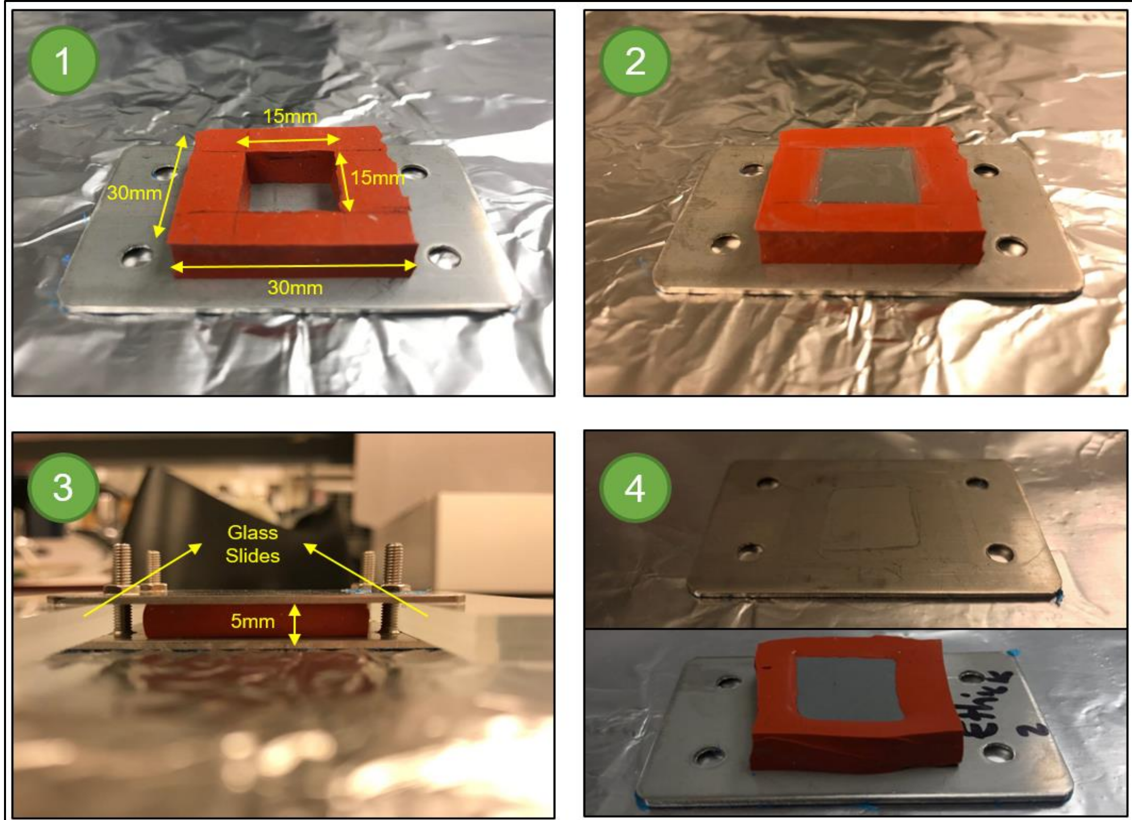

Figure A3. Sample preparation steps for the fracture strength characterization of the bonding between epoxy to the steel plates: (1) The silicone gasket is cut and pressed on top of the steel plate. (2) The epoxy is poured inside of the cavity and the top surface is swiped with a blade. (3) Another layer of steel plate is placed on top of the silicone gasket. The plate is screwed and tighten with five 1 mm thick glass slides in between the steel plates to make sure that the steel plates are parallel. (4) After the tensile test, as expected, the sample was broken from the epoxy-steel bonding area. The measured fracture strength for epoxy-steel plate bonding area is ~3MPa.

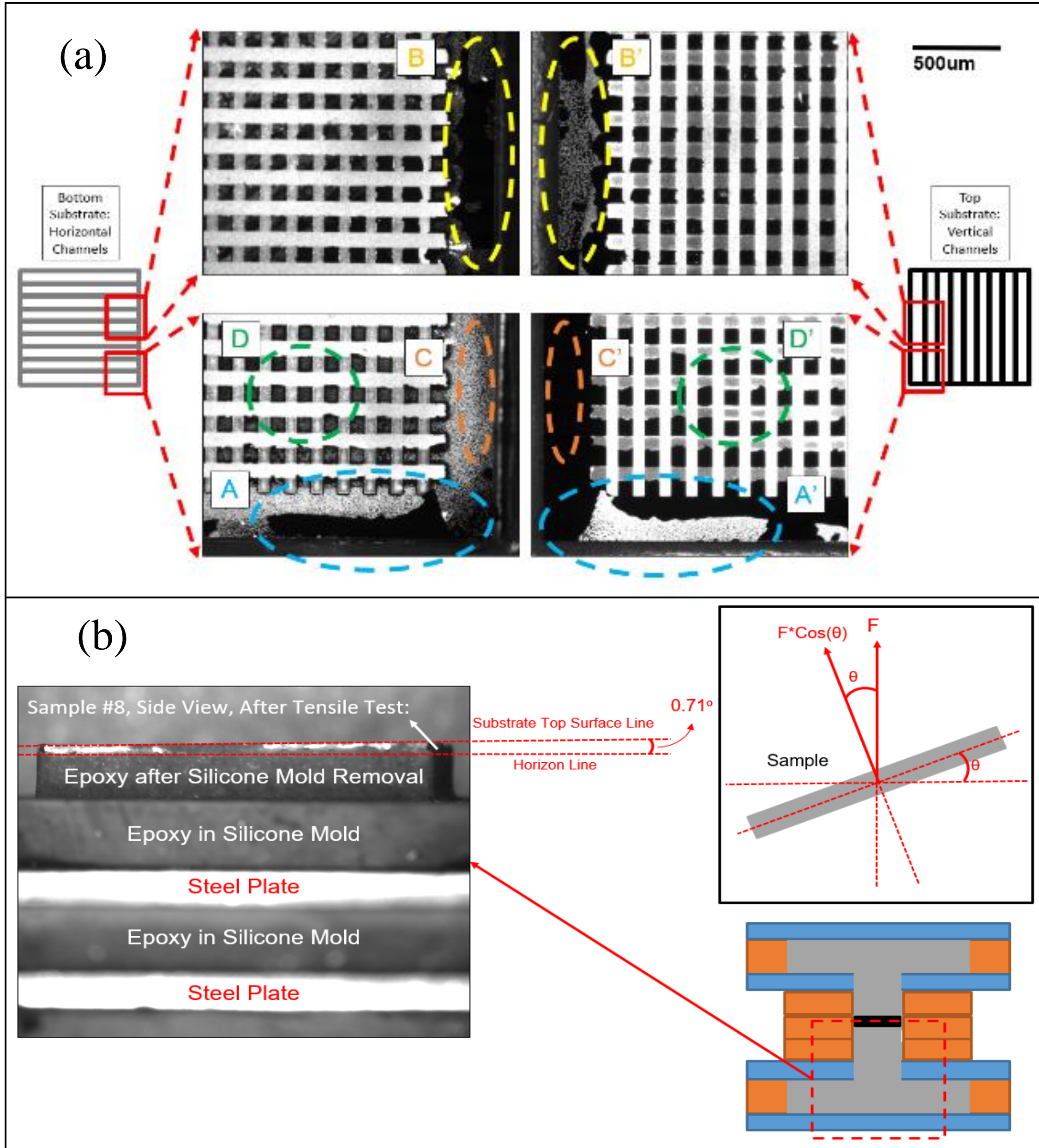

Figure A4. Sample surface after the tensile test: (a) The leftover particles are visible using optical microscope imaging over the top and the bottom substrates depending on the crack initiation location in the bonding section. (b) Substrate angles were measured for all of the samples (with 0.01° precision). Error in the tensile force measurement from angle misalignment (F vs. $F \times \cos(\theta)$) for Au-Sn samples was ~0.04%. Load Measurement Accuracy of the tensile testing tool was ± 0.4%.

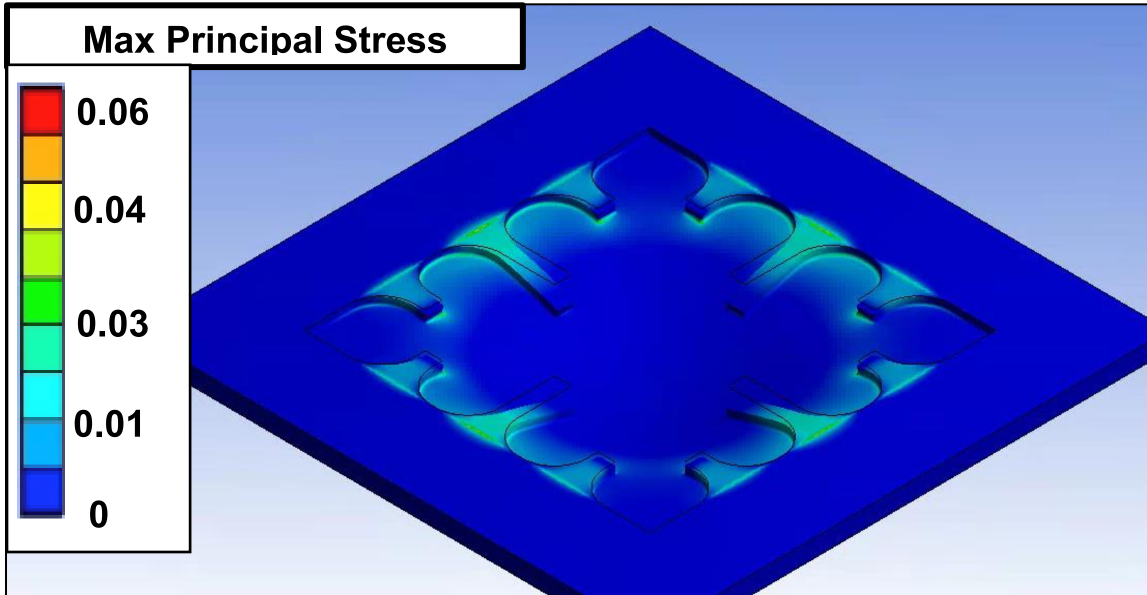

Figure A5. Ribs reduce the effective cavity radius and increase the effective cavity thickness. However, an equivalent force should be tolerated in the roots (i.e. the radius reduction advantage is not applicable in the roots), which have a smaller area compared with the original cavity edge. This results in a higher tensile stress concentration. Increasing the area of the roots using fillets helps with the stress reduction, however; it will be equivalent to reducing the cavity area and is not applicable in the parametric study of the rib support structures.